

THESIS

COMPUTATIONAL MODELING OF WIND TURBINE WAKE INTERACTIONS

Submitted by

Cole J. Davis

Department of Civil and Environmental Engineering

In partial fulfillment of the requirements

For the Degree of Master of Science

Colorado State University

Fort Collins, Colorado

Spring 2012

Master's Committee:

Advisor: S. Karan Venayagamoorthy

Co-Advisor: Paul R. Heyliger

Eric D. Maloney

ABSTRACT

COMPUTATIONAL MODELING OF WIND TURBINE WAKE INTERACTIONS

The rapid expansion of the wind energy market necessitates the need for advanced computational modeling and understanding of wind turbine aerodynamics and wake interactions. The following thesis work looks to study turbulence closure methods widely used in computational fluid dynamics (CFD) and their applicability for modeling wind turbine aerodynamics. The first investigation is a parametric study of turbulence models and their performance on geometries of stationary in-line turbines and disks spaced at different intervals. A variety of Reynolds-averaged Navier-Stokes (RANS) closure schemes (Spalart-Allmaras, Standard $k-\varepsilon$, $k-\varepsilon$ Realizable, $k-\varepsilon$ RNG, Standard $k-\omega$, $k-\omega$ SST) were studied as well as a large eddy simulation (LES) with a dynamic Smagorinsky-Lilly sub-grid scale (SGS) model. The simulations showed the grid refinement to be inadequate for LES studies. The RANS closure schemes did not indicate a dominant model. However, relevant literature on separating flows has shown the $k-\omega$ SST model to be preeminent.

The second investigation uses only the $k-\omega$ SST RANS closure scheme to model wake development and resolution for both a single fully resolved rotating turbine as well as two in-line fully resolved rotating turbines. These simulations were successful in predicting wake development and resolution, as well as predicting velocity deficits

experienced by the downstream turbine. Vorticity results also showed an accurate wake structure and helical tendencies.

In the third investigation, a grid independence study was performed to gain an accurate pressure distribution on the blade surfaces for a separate, collaborative, non-linear, structural study of wind turbine blades. This study showed a strong asymptotic relationship of the maximum pressure on the blades to the predicted Bernoulli pressure on the blade.

The results of this research show clear wake development, structure and resolution. The velocity deficits found translate directly in to power deficits for downstream turbines and the vorticity translates directly into increased fatigue experienced by the blades.

In contrast to the vast super-computer simulations found in literature, all simulations in this thesis work were calculated using four parallel processors. The accuracy was achieved through assumptions, which were designed to maintain the desired physics while simplifying the complexity of the problem to the capabilities of desktop computing. This research demonstrates the significance of model design and capabilities and accuracy achievable using desktop computing power. This has vast implications of accessibility into academia and the further development of the wind power industry.

ACKNOWLEDGEMENTS

Funding for this research was provided by a seed grant from the Center for Research and Education in Wind (CREW). Jordan Wilson provided a significant amount of modeling assistance and consultation. Dr. Paul Heyliger performed all the structural simulations. Dr. S. Karan Venayagamoorthy provided excellent guidance throughout the thesis work.

TABLE OF CONTENTS

Abstract	ii
Acknowledgements	iv
Table of Contents	v
Table of Figures	viii
Table of Tables	xii
Symbols and Abbreviations	xiii
Chapter 1. Introduction.....	1
1.1 Background	2
1.1.1 Modern Wind Turbines	3
1.1.2 Orientation.....	4
1.1.3 Rotational Speed.....	5
1.1.4 Rotor Characteristics	6
1.1.5 Aerodynamic Power Control.....	7
1.1.6 Rotor and Blade Aerodynamics	8
1.1.7 Other Design Considerations.....	8
1.2 Objective	9
1.3 Thesis Layout.....	11
Chapter 2. Literature review	13

2.1	Blade Element Momentum Theory	13
2.2	Elementary Wind Models.....	20
2.3	Power Curves	31
2.4	CFD Wind Turbine Models.....	35
2.5	Summarizing Remarks	45
Chapter 3. Parametric Study.....		47
3.1	Theory	48
3.1.1	Spalart-Allmaras Model	49
3.1.2	Standard $k-\varepsilon$ Model.....	50
3.1.3	$k-\varepsilon$ Realizable Model	51
3.1.4	$k-\varepsilon$ RNG Model	52
3.1.5	Standard $k-\omega$ Model	53
3.1.6	$k-\omega$ SST Model.....	55
3.1.7	LES	56
3.2	Model Description	57
3.3	Results.....	59
3.4	Summarizing Remarks.....	65
Chapter 4. Rotating Turbine Study.....		67
4.1	Wake Interaction Model Description.....	67
4.2	Wake Interaction Results	69
4.3	Grid Independence Model Description.....	74
4.4	Grid Independence Results	75
4.5	Discussion on Structural Application	77

4.6	Summarizing Remarks.....	80
Chapter 5.	Conclusions.....	82
5.1	Summary.....	82
5.2	Key Results.....	83
5.3	Suggestions for Further Research.....	85
	References.....	87

TABLE OF FIGURES

Figure 1	Power projection from new plants in 2016 (Ball, 2011).	4
Figure 2	Aerial view from the Southeast of wake clouds at Horns Rev on February 12, 2008 (© Vattenfall, Horns Rev 1 owned by Vattenfall. Photographer Christian Steiness) (Emeis, 2010).....	10
Figure 3	Assumed stream lines over the rotor, velocity and pressure up and downstream of the rotor (Hansen, 2008).....	14
Figure 4	Cylindrical control volume around a wind turbine (Hansen, 2008).	15
Figure 5	Trends of C_P and C_T with maximum C_P and α shown for an ideal HAWT (Hansen, 2008).	18
Figure 6	Logarithmic boundary layer velocity profiles for varying roughness coefficient, with a reference wind speed of 13.4 m/s.	22
Figure 7	Points around a turbine where velocity history is typically calculated (Hansen, 2008).	27
Figure 8	Representative power coefficient versus wind speed curves for constant speed and variable speed HAWTs (Leishman, 2006).	33
Figure 9	Power Curve for NREL 5MW reference turbine (Jonkman, et al., 2009).....	33
Figure 10	Comparison of power curves. Exact (solid line). IEC (filled triangles). Dynamic (open squares with error bars) (Gottschall & Peinke, 2007).	34

Figure 11	Distribution of turbulence intensity in wake for empirical model (left), and idealized results of CFD study (right) (Hahm & Wußow, 2006).	36
Figure 12	Streamwise velocity profiles (m/s): wind tunnel measurements (\circ), ADM-NR (dashed line), ADM-R (solid line), ALM (dotted line) (Porté-Agel, et al., 2011).	40
Figure 13	Schematic showing a one-dimensional array of two horizontal axis wind turbines.	47
Figure 14	Cut-away of meshed domain for $\alpha = 10$ (left) and meshed turbine (right).	58
Figure 15	Velocity profiles (m/s) for selected turbulence models over two in-line stationary turbines spaced $5D$	60
Figure 16	Streamwise velocity contours (m/s) on vertical bisecting plane for turbine spacings αD ($\alpha\{5, 10, 15\}$) $k-\omega$ SST.	61
Figure 17	Streamwise velocity profiles $1D$ upstream of the second stationary turbine for spacings αD ($\alpha\{5, 10, 15\}$) $k-\omega$ SST.	61
Figure 18	Streamwise velocity profiles $1D$ downstream of each stationary turbine for spacings αD ($\alpha\{5, 10, 15\}$) $k-\omega$ SST.	62
Figure 19	Vorticity magnitude (1/s) contours on horizontal plane, bisecting turbine hubs for spacings αD ($\alpha\{5, 10, 15\}$) $k-\omega$ SST.	62
Figure 20	Vorticity magnitude on horizontal plane, bisecting turbine hubs, showing vorticity $1D$ up- and downstream of each turbine. Spacings αD ($\alpha\{5, 10, 15\}$) $k-\omega$ SST.	63

Figure 21	Velocity profiles (m/s) for selected turbulence models over two in-line non-porous disks spaced 5D	64
Figure 22	Streamwise velocity contours (m/s) on vertical bisecting plane for disk spacings αD ($\alpha\{5, 10, 15\}$) for $k-\omega$ SST.	64
Figure 23	Vorticity magnitude (1/s) contours on horizontal plane, bisecting turbine hubs for spacings αD ($\alpha\{5, 10, 15\}$) $k-\omega$ SST.	65
Figure 24	Cut-away of meshed domain for $\alpha = 5$ (left) and meshed turbine enclosed in rotating domain (right).	68
Figure 25	Velocity profiles (m/s) for $k-\omega$ SST and spacing of 5D , comparing the stationary turbine, rotating turbine, and non-porous Disk.	69
Figure 26	Streamwise velocity contours (m/s) on vertical bisecting plane comparing two turbines spaced 5D and single turbine with 20D spacing downstream, $k-\omega$ SST was used.	70
Figure 27	Velocity profiles (m/s) comparing single turbine with 20D spacing downstream to two turbines spaced 5D with 15D spacing behind second turbine, $k-\omega$ SST was used.	70
Figure 28	Vorticity magnitude (1/s) on horizontal plane bisecting turbine hubs, for in-line turbines 5D spacing (top), single turbine 20D spacing downwind (bottom).	71
Figure 29	Vorticity magnitude iso-surfaces (blue = 0.12 1/s, magenta = 0.13 1/s, green = 0.14 1/s), for in-line turbines 5D spacing (top), single turbine 20D spacing downwind (bottom).	72

Figure 30	Vertical velocity (m/s) contours on horizontal plane bisecting turbine hubs, for in-line turbines 5D spacing (top), single turbine 20D spacing downwind (bottom).	72
Figure 31	Non-dimensionalized streamwise velocity profiles 2D downstream of turbine, comparison between current study and data extracted from highly resolved LES simulations (Porté-Agel, et al., 2011).....	74
Figure 32	Pressure (Pa) vs. mesh size. Maximum pressure is asymptotic to Bernoulli pressure as mesh size increases (left). Average pressure is asymptotic as mesh size increases (right).....	76
Figure 33	Pressure distribution on blades (Pa).....	77
Figure 34	Load vs. tip deflection for linear Euler-Bernoulli, non-linear higher order, and non-linear 2D Lagrangian beam solutions (Heyliger, et al., 2011).....	79
Figure 35	Radial distance vs. transverse deflection results of non-linear Lagrangian analysis.....	79

TABLE OF TABLES

Table 1	Typical values of z_0 and m	21
Table 2	Grid independence mesh restrictions.....	75

SYMBOLS AND ABBREVIATIONS

ABL	Atmospheric Boundary Layer
ADM	Actuator Disk Model
ADM-NR	Actuator Disk Model - Non Rotating
ADM-R	Actuator Disk Model - Rotating
ALM	Actuator Line Model
BEM	Blade Element Method
CFD	Computational Fluid Dynamics
CPU	Central Processing Unit
D	Rotor diameter
DES	Detached Eddy Simulation
DNS	Direct Numerical Simulation
FEM	Finite Element Method
FSI	Fluid-Structure Interaction
HAWT	Horizontal Axis Wind Turbine
IEC	International Electrotechnical Commission
k	Turbulent kinetic energy
LASDD	Locally Averaged Scale-Dependent Dynamic
LES	Large Eddy Simulation
LLJ	Low-Level Jet
NREL	National Renewable Energy Laboratory
NURBS	Non-Uniform Rational B-Splines
PBL	Planetary Boundary Layer
RANS	Reynolds-Averaged Navier-Stokes
RBVMS	Residual-Based Variational Multiscale
RNG	Renormalization Group
SA	Spalart-Allmaras
SODAR	Sonic Detection and Ranging
SST	Shear-Stress Transport
VAWT	Vertical Axis Wind Turbine
VTM	Vorticity Transport Model
ε	Rate of dissipation of turbulent kinetic energy
ω	turbulence frequency

CHAPTER 1. INTRODUCTION

As concerns continue to increase over resource availability, energy prices, environmental impacts, and worldwide population growth, renewable energy production becomes paramount in maintaining current energy demands and meeting future requirements. Wind energy has prevailed as the most cost-effective source of renewable energy production. Within the United States, energy production from wind is aimed at 20% of the total energy market by 2030 (USDOE, 2008). As wind turbines reach higher into the atmosphere, rotor diameters increase and wind farms can expand beyond 20 km in length. Understanding the flow dynamics imposed by the atmospheric boundary layer (ABL) and local turbine wake interactions is an essential part of wind farm design and optimization. The turbine wakes not only decrease the downstream mean velocity resulting in power production losses, but also increase fluctuations, which leads to structural fatigue.

It is the intent of this thesis to: 1) demonstrate a thorough review of progress in relevant fields through a literature review; 2) investigate through computational fluid dynamics (CFD) studies the applicability of different Reynolds-averaged Navier-Stokes (RANS) turbulence models and 3) examine the wake development and resolution of two in-line rotating turbines with mind toward the effects of their subsequent fatigue loading of the turbine blades.

1.1 BACKGROUND

Wind power has a rich history that began with the powering of ship sails and has developed into its current dominance in the wind power industry. The first recognizable wind energy conversion systems were developed in the fifteenth century for grinding and milling grain. These early windmills saw improvements as advanced as twisted blades. In the eighteenth century, Dutch settlers brought the iconic wind fan to the United States where it was used to pump water on ranches. In the early twentieth century, wind turbines began being used for power generation; however, it was not until the 1970's oil crisis that windmills started to become popular as a substitute for oil-based energy. . Today, global warming is the primary incentive fueling the development and implementation of wind power (Leishman, 2006).

The rapid development of wind turbine technology necessitated the need for more accurate analysis. Traditionally this analysis was borrowed and modified from the analysis used for helicopter aerodynamics because there are several similarities between the operation of helicopter blades and windmill blades. These similarities have allowed for the prediction and comprehension of unsteady blade-air loads, and turbine performance in attached and stalled flow. They have also allowed for the prediction of structural loads and the aeroelastic response of rotating blades. However, the application of helicopter aerodynamics to wind turbine aerodynamics is limited. For example, there are many atmospheric conditions that wind turbines experience that helicopters do not. These conditions include ground boundary layer effects, atmospheric turbulence, large turbulent eddies, temporal and spatial variations in wind shear, and thermal convection

and stratification. There are also unnatural conditions unique to wind turbines. These include unsteady wake effects from tower shadow and effects from upstream towers.

Much has been learned from the study of helicopter aerodynamics. The main analysis method that has been borrowed is the blade element momentum (BEM) theory with the addition of inflow models (Leishman, 2006). This method has been very useful. However, with advancements in computing power, CFD is becoming a more popular analysis method (McGowan, 2000). The following sections discuss further wind turbine considerations.

1.1.1 MODERN WIND TURBINES

. In the past, power generated from sources like coal, natural gas, nuclear fuel was considerably cheaper than wind power. However, with increases in fossil fuel costs and improvements in wind turbine technology, the playing field is starting to level (McGowan, 2000). As shown in Figure 1, the Wall Street Journal has suggested by 2016 that the cost of energy from a new wind farm will cost about as much as energy from a new natural gas power plant in the windiest regions and the same as energy from new coal fired power plants in most regions (Ball, 2011). As a result of the increased demand for wind turbine technology, modern wind turbines have increased in size and capacity considerably in the last several years. A wind turbine rotor diameter can vary between five meters and one hundred meters, however typically they are greater than fifty meters in diameter. Their power generating capability also varies greatly with some turbines producing just a few kilowatts and others producing a few megawatts (McGowan, 2000)

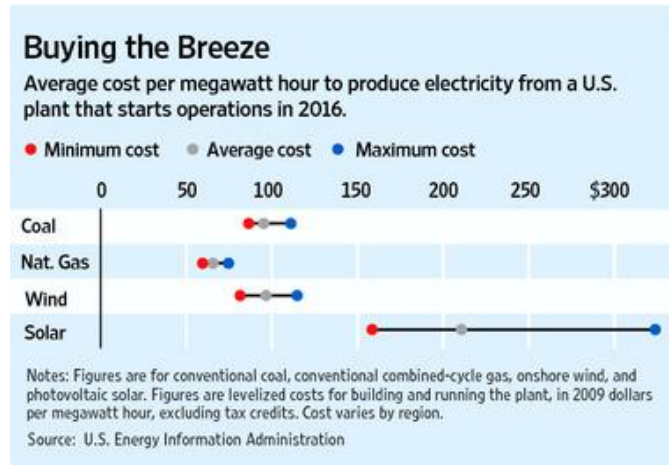


Figure 1 Power projection from new plants in 2016 (Ball, 2011).

1.1.2 ORIENTATION

There are two orientations of wind turbines: horizontal axis wind turbines (HAWT) and vertical axis wind turbines (VAWT). There are advantages and disadvantages to each orientation. VAWTs use drag forces to rotate their blades and are frequently referred to as drag machines. The dominant advantage to a VAWT is that it can accept wind from any direction at any time. This means that it does not require any yaw system to align the turbine in the direction of the incident wind field. The blades are commonly straight without any taper along the long axis. This allows them to be manufactured at lower cost. Since they rotate about the vertical axis the drive train can be located near the ground, which reduces the maintenance costs. Although VAWTs can accept wind from any direction, they are less efficient than HAWTs. Another major problem with VAWTs is their scalability in terms of viability for commercial production. They also tend to see larger fatigue damage on the blades at the rotor as a result of cyclic aerodynamic stresses (McGowan, 2000).

In contrast, HAWTs use lift forces to rotate their blades and are frequently referred to as lift machines. HAWTs can be designed such that the turbine is either

upstream or downstream from the supporting tower. In the downstream version, the turbine automatically aligns its self with the wind; this rotation is known as yaw. To assist with their free yawing capability, the rotor blades are coned slightly in the downwind direction. Downstream HAWTs are influenced by tower wind shadow. Since the supporting tower is upstream of the rotor, a wake is created by the tower. The main effect of this wake is uneven air loading on the blades, which causes an uneven angle of attack on the blades and leads to decreased efficiency. In addition, the uneven cyclic loading causes fatigue damage not only to the blades but to the tower and drive train as well. To a lesser extent the downwind orientation also causes increased noise output.

In the upstream version, all tower wake effects are eliminated. However, the turbine is not capable of free yawing. This means that an active yaw control system is needed. These systems require a yawing motor, gears and a brake to hold the turbine in place when it is optimally oriented into the wind. Along with the increased complexity of a yaw control system, an increased torsional load is applied to the tower (McGowan, 2000).

A large advantage to HAWTs is the issue of solidity, which is defined as the ratio of the blade area to the swept blade area. As the turbine gets larger, the solidity gets smaller, which in-turn reduces the cost per kilowatt. HAWTs are also easier to mount on top of a large tower, which reduces the initial investment cost. As a result, HAWTs currently dominate the wind power market (McGowan, 2000).

1.1.3 ROTATIONAL SPEED

There are two types of rotors: fixed speed rotors and variable speed rotors. The entire design of a fixed speed rotor is based on the requirements of the generation system

and the gearbox. This type of design can experience decreased efficiency when wind speeds are not optimal. Fixed speed rotors make up the majority of wind turbines currently in use, however variable speed rotors are gaining in market share (McGowan, 2000).

Variable speed rotor designs allow for more wind energy to be captured. They also reduce the loading on the rotor and drive train components. Because variable speed rotors produce variable power output, power electronic converters are required for a turbine to be tied into the grid. Power electronic converters change the power output to the voltage and frequency required for transmission on the grid. They also allow a more flexible choice in generator. With this new option, a generator can be chosen for low-speed operation, increasing the range of sites on which wind turbines can be erected (McGowan, 2000).

1.1.4 ROTOR CHARACTERISTICS

Rotor design and analysis is largely focused on maximizing the power coefficient as a function of tip-speed ratio. The tip-speed ratio is the ratio of the blade tip-speed to incoming wind speed. This ratio is also directly related to solidity which reduces the cost of power generation. As a result, a longer blade produces a greater tip-speed ratio and a higher the rotational speed. A greater rotational speed lowers the torque on the drive train for a given power output. This increase in rotational speed, however, is noisier and increases the fouling of the blade (buildup of insects and dirt on the leading edge of the blade which increases the frictional coefficient) (McGowan, 2000).

While typical rotors are designed with three blades, some rotors have only two. Rotors designed with three or more blades have a constant polar moment of inertia with

respect to yawing. This allows for smooth yawing operations. Two rotor blade designs have a lower polar moment of inertia when the rotors are vertical and a higher polar moment of inertia when the rotors are horizontal. This oscillation causes cyclic loading and increased fatigue damage (McGowan, 2000).

1.1.5 AERODYNAMIC POWER CONTROL

Because high winds can cause damage to wind turbines, they need to be designed with aerodynamic controls to maintain power. These controls include stall control, variable pitch control and yaw control. Stall control alters the wind's angle of attack on the blades of the rotor. This is generally accomplished by the introduction of an induction generator. Stall control is commonly coupled with blades that are fastened rigidly to the hub. While maximum power generation is achieved at increased wind speeds, there is some power loss at lower wind speeds. The stall control method is not sufficient during extreme wind events, so an additional mechanical break is necessary to prevent damage (McGowan, 2000).

Variable pitch control is accomplished by changing the angle of the blades along their long axis. This decreases the lift force available to turn the rotor and allows for more control than a stall control. Variable pitch control requires a more complicated hub assembly in order to have the desired mechanical control. As a variation on the full blade pitch control there are some designs that have an option for partial span pitch control (McGowan, 2000).

Yaw control achieves aerodynamic power control by turning the rotor away from the dominant wind direction. This method requires a very robust yaw control system able to operate with increased torques. The hub must also be able to withstand high

gyroscopic air loads. Yaw control is generally only implemented on small wind turbines so that the increased structural requirements can be minimized (McGowan, 2000).

1.1.6 ROTOR AND BLADE AERODYNAMICS

Recently the National Renewable Energy Laboratory (NREL) designed a series of ten blades to address issues surrounding wind turbine aerodynamics. This new series of blades are insensitive to blade surface roughness, which means that fouling is not a consideration. The series was also designed to address the needs of stall, variable pitch, and variable rotation control. Contemporaneous with the production of the NREL blades, Risø National Laboratory in Europe designed a series of six blades. This series is also insensitive to surface roughness. They were able to achieve lift coefficients of 1.5 and high lift-to-drag ratios for high angles of attack. Another feature of the Riso blades was the implementation of trailing edge stall capabilities (McGowan, 2000).

Traditionally, aerodynamic analysis has been performed using the BEM theory with codes like AeroDyn and FAST (Jonkman & Buhl Jr., 2005). However, in recent years CFD has become predominant in academic research. An extensive review of CFD wind turbine studies will be presented in Chapter 2 (section 2.4).

1.1.7 OTHER DESIGN CONSIDERATIONS

Several other design considerations include the categories of maintenance, environmental concerns, and wind resources. Maintenance can make up a significant portion of the overall cost of a wind turbine as maintenance costs tend to increase through the lifespan of the wind turbine. A benefit of increased turbine size is a decreased projected maintenance cost. Maintenance and capital cost can also be highly dependent on local labor and expertise.

Environmental concerns include noise pollution, aviation migration patterns, land use restrictions, local opposition, and electromagnetic interference (McGowan, 2000).

Wind resources need to be studied in depth before the implementation of any wind turbines. The higher the wind in the area, the more desirable the location; wind classes are based on power density and mean wind speed. Wind classes vary from class 1 to class 5, with class 1 being the least optimal for power production and class 5 being the most optimal. A wind class of at least 4 is required for a turbine to be reasonably productive (Elliott, et al., 1986). High wind environments also come with their issues. Because high wind may not always be constant, the variability of wind speeds may need to be studied. Higher wind areas also frequently have increased wind shear, gusts, and turbulence, all of which cause increased fatigue damage to wind turbines. Topography also plays a major role in wind patterns. This coupled with vegetation variations can cause greater surface roughness, requiring the supporting tower to be taller to get into the desired boundary layer level (McGowan, 2000).

1.2 OBJECTIVE

With the ever increasing number of turbines in wind farms on- and off-shore, it is becoming progressively more critical to understand turbine interactions. As flow passes over a turbine, the turbulence intensity increases and inherently magnifies the fatigue loading on downstream turbines. In addition, velocity deficits in turbine wakes can drastically affect downstream power production since power is proportional to the cube of velocity. The complexity of turbine flow mechanics significantly increases when more than one turbine is considered, and that is the thrust of this work.



Figure 2 Aerial view from the Southeast of wake clouds at Horns Rev on February 12, 2008 (© Vattenfall, Horns Rev 1 owned by Vattenfall. Photographer Christian Steiness) (Emeis, 2010).

Figure 2 shows a now-famous photograph of the Horns Rev wind farm in Denmark, and illustrates the wake interactions in large farms. During a previous study at Horns Rev wind farm, velocity deficits downstream of the turbines were found to be in excess of 20% for both crosswind and aligned wind directions (Christiansen & Hasager, 2006). With wake effects of this magnitude, it is critical that turbine interactions be better understood and more accurately modeled. With a better understanding of wind turbine wake interactions and improved modeling techniques, wind farms can be designed to better optimize power output and minimize fatigue damage, bringing down their operating cost and increasing their revenue potential. Therefore it is the objective of this thesis work to study the applicability of different turbulence models, and the

development and resolution of the wakes of two in-line HAWTs, with mind toward the fatigue loading of turbines through CFD modeling.

This will be accomplished in the following three parts:

- Part 1: A parametric study of CFD turbulence models on stationary turbines and disks;
- Part 2: A CFD study of rotating wake development and resolution; and
- Part 3: A CFD study of grid independence with regard to pressure on the turbine blades.

All the parts of this study were performed using ANSYS FLUENT, a finite volume commercial CFD code (ANSYS, 2010). The purpose of Part 1 is to determine the applicability of the commonly used turbulence models built into ANSYS FLUENT for the problem of wind turbine fluid mechanics. Part 2 addresses the more complex problem of the rotating turbines, and investigates the development, resolution, and interaction of turbine wakes. In Part 3, the pressure distribution on the blade surfaces is accomplished through a grid independence study. This pressure distribution was then input into a separate collaborative structural model. By modeling the wake interaction and blade loading, wind turbine spacing can be optimized to maximize power output and minimize fatigue loading.

1.3 THESIS LAYOUT

The technical portion of this thesis is divided into four chapters. Chapter 2 presents a literature review of relevant scholarly publications. This information is presented as both conceptual descriptions as well as case study discussions. The research

provided in this Chapter builds a strong foundation for understanding current methods for the study of wind turbines.

Chapter 3 investigates the applicability of commonly used commercial CFD turbulence closure methods to the problem of wind turbine wake modeling. This is accomplished both through a literature review of turbulence closure methods, as well as a parametric study of turbulence models using CFD simulations of flow over stationary turbines and stationary disks. The performance of the turbulence models was assessed and an appropriate model was chosen for further study.

Chapter 4 builds upon the parametric study by continuing with the appropriate turbulence closure method, and using it in simulations of rotating turbines. These rotating simulations give insight into the wake structure, formation, interaction with downstream turbines, and resolution.

Chapter 4 continues with a grid independence study, comparing the asymptotic maximum blade pressure to the calculated maximum Bernoulli pressure. Load distributions on the turbine blades are then one-way coupled to a separate collaborative structural study. A brief explanation of this coupled structural study is provided.

Chapter 5 summarizes and concludes the main results and findings of this thesis work. Future direction and areas of study are also discussed.

CHAPTER 2. LITERATURE REVIEW

It is the intent of the literature review to encompass the subject matter critical for understanding and comprehensively modeling wind turbine wake interactions. The literature review will cover the blade element momentum theory, elementary wind models, power curves, and previous CFD studies.

2.1 BLADE ELEMENT MOMENTUM THEORY

The Blade Element Momentum (BEM) model is the most fundamental method for wind turbine analysis. Originally developed by Glauert in 1935 for analysis of airplane propellers, it is a one-dimensional approach that models thrust as a function of wind speed (Glauert, 1935). The principal function of the BEM model is to determine the conditions for maximum energy conversion (Leishman, 2006). There are several assumptions that are necessary to make the BEM method valid. They include a frictionless, incompressible, steady flow with no rotational velocity component. The rotor is modeled as a permeable disk, and there are no external forces that act on the fluid upstream or downstream of the rotor. Drag is obtained by modeling a pressure drop over the rotor (Hansen, 2008). Figure 3 shows the assumed conditions of the standard BEM model.

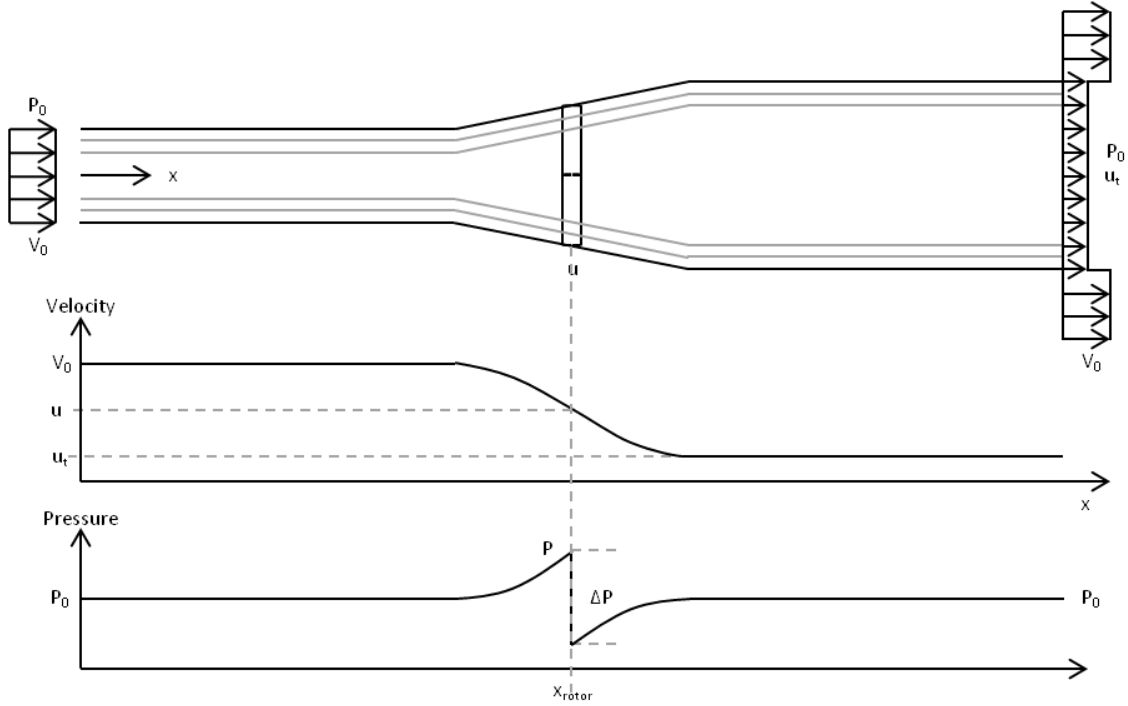


Figure 3 Assumed stream lines over the rotor, velocity and pressure up and downstream of the rotor (Hansen, 2008).

With these assumptions for an ideal rotor, the relationships between the velocities V_0 , u , and u_t (where V_0 is the upstream velocity, u is the velocity at the rotor, and u_t is the velocity in the wake downstream of the rotor), the thrust, T , and power, P can be derived. The thrust force is,

$$T = \Delta p A, \quad \text{Equation 1}$$

where A is the swept area of the rotor.

Based on these assumptions, it is easy to apply Bernoulli's equation twice for the flow upstream to the rotor and from the rotor to the downstream flow. This gives:

$$p_0 + \frac{\rho V_0^2}{2} = p + \frac{\rho u^2}{2}, \quad \text{Equation 2}$$

$$(p - \Delta p) + \frac{\rho u^2}{2} = p_0 + \frac{\rho u_t^2}{2}. \quad \text{Equation 3}$$

Combining Equations 2 and 3, Δp can be obtained as:

$$\Delta p = \frac{\rho}{2}(V_0^2 - u_l^2). \quad \text{Equation 4}$$

With this relationship known, the axial momentum equation,

$$\frac{d}{dt} \iiint_{CV} \rho u(x, y, z) dx dy dz + \iint_{CS} u(x, y, z) \rho \vec{V} \cdot \vec{dA} = F_{ext} + F_{press}, \quad \text{Equation 5}$$

can be examined. This can be simplified by viewing the control volume, Figure 4.

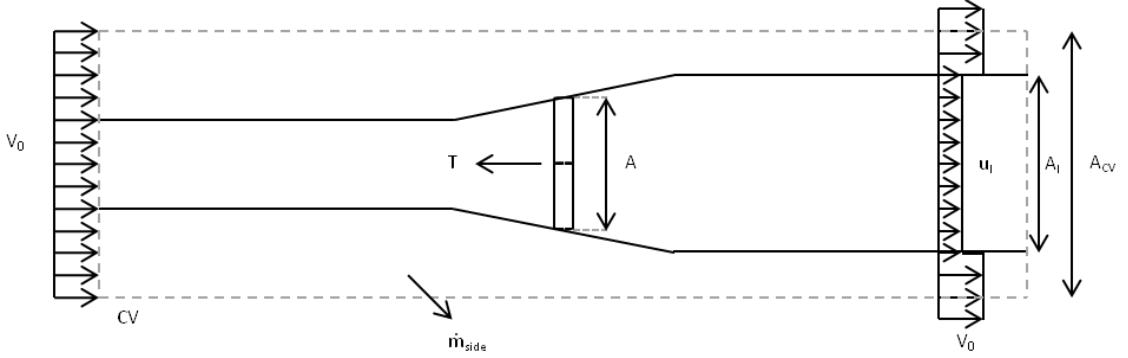


Figure 4 Cylindrical control volume around a wind turbine (Hansen, 2008).

Since the flow is assumed to be steady, the first term in the momentum equation is zero. F_{ext} represents the pressure on both ends. Since the pressure is equal and it acts on the same area, F_{ext} is zero. F_{press} is the axial component of the pressure acting on the lateral boundary of the control volume. There is no axial pressure on the lateral boundary. \vec{dA} is a vector normal to the control surface with a length equivalent to the infinitesimal area of the element. With these simplifications the momentum equation becomes,

$$\rho u_l^2 A_l + \rho V_0^2 (A_{CV} - A_l) + \dot{m}_{side} V_0 - \rho V_0^2 A_{CV} = -T, \quad \text{Equation 6}$$

\dot{m}_{side} can be solved for by applying conservation of mass principles.

$$\begin{aligned} \rho u_l A_l + \rho V_0 (A_{CV} - A_l) + \dot{m}_{side} &= \rho V_0 A_{CV} = -T, \\ \dot{m}_{side} &= \rho A_l (V_0 - u_l). \end{aligned} \quad \text{Equation 7}$$

Conservation of mass can also relate A and A_l . This results in,

$$\dot{m} = \rho u A = \rho u_l A_l. \quad \text{Equation 8}$$

By combining Equations 6, 7, and 8,

$$T = -\rho u_l A_l (V_0 - u_l) = \dot{m}(V_0 - u_l), \quad \text{Equation 9}$$

the thrust can be solved. Substituting Equations 1, 4, and 8,

$$\frac{\rho}{2}(V_0^2 - u_l^2)A = \rho u A (V_0 - u_l),$$

$$u = \frac{1}{2}(V_0 + u_l), \quad \text{Equation 10}$$

u can be solved. This shows that the velocity flowing over the turbine is the mean between the upstream and downstream velocities.

Since the system is assumed to be frictionless it follows that there is no loss of internal energy. This yields the equation for the potential power captured as,

$$P = \dot{m} \left(\frac{1}{2} V_0^2 + \frac{p_0}{\rho} - \frac{1}{2} u_l^2 - \frac{p_0}{\rho} \right),$$

$$P = \frac{\rho u A}{2} (V_0^2 - u_l^2). \quad \text{Equation 11}$$

It is at this point that it is appropriate to introduce the simplification of an induction factor, $a = 1 - \frac{u}{V_0}$. It follows that,

$$u = (1 - a)V_0, \quad \text{Equation 12}$$

$$u_l = (1 - 2a)V_0, \quad \text{Equation 13}$$

The power equation can be written in terms of a as,

$$P = \frac{\rho(1 - a)V_0 A}{2} (V_0^2 - (1 - 2a)^2 V_0^2),$$

$$P = 2\rho A V_0^3 a(1 - a)^2. \quad \text{Equation 14}$$

The thrust equation can also be written in terms of a as,

$$T = \rho(1 - a)V_0 A (V_0 - (1 - 2a)V_0),$$

$$T = 2\rho AV_0^2 a(1 - a). \quad \text{Equation 15}$$

The power and thrust can both be non-dimensionalized in terms of a power coefficient and a thrust coefficient. The power coefficient is the ratio of power to the amount of power available, P_{avail} , over the swept cross-sectional area. This reduces as,

$$C_P = \frac{P}{P_{avail}},$$

$$C_P = \frac{2\rho AV_0^3 a(1 - a)^2}{\frac{1}{2}\rho AV_0^3},$$

$$C_P = 4a(1 - a)^2. \quad \text{Equation 16}$$

Likewise the thrust coefficient is the ratio of thrust to the amount of thrust available, T_{avail} , over the swept cross-sectional area. This reduces as,

$$C_T = \frac{T}{T_{avail}},$$

$$C_T = \frac{2\rho AV_0^2 a(1 - a)}{\frac{1}{2}\rho AV_0^2},$$

$$C_T = 4a(1 - a). \quad \text{Equation 17}$$

The BEM method is very sensitive to the value of a . Since the thrust and power cannot exceed their available amount it can be inferred that C_T and C_P cannot exceed one. This is not a problem for the coefficient of thrust, as its value will be less than one for any value of a . However, the coefficient of power requires a not to exceed 1.42. This is an illogical value since the velocity over the turbine cannot be negative or greater than the upstream velocity. This requirement limits a to greater than zero and less than one. The controlling limit comes from the assumption of constant streamlines. When a exceeds 0.4, the momentum theory is no longer valid, and the free shear layer in the wake becomes unstable and large eddies form in the wake resulting in negative velocities. This

is known as a turbulent wake state. A turbulent wake state invalidates many of the assumptions on which the BEM method is based. Figure 5 shows the relationship between a and C_p and C_T .

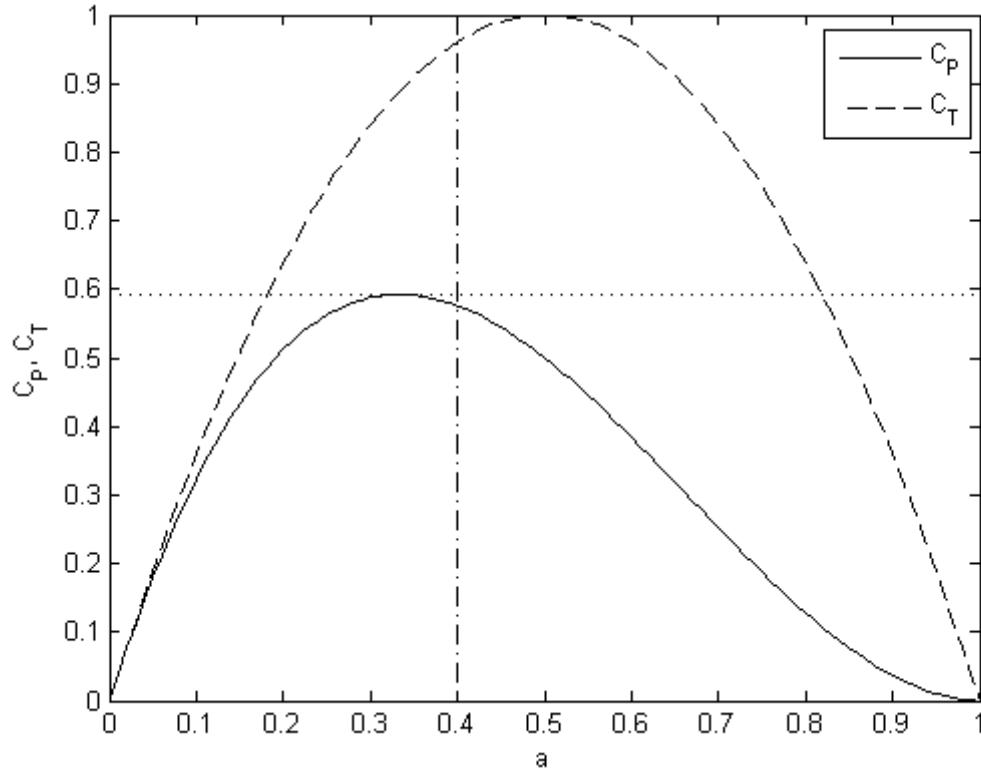


Figure 5 Trends of C_p and C_T with maximum C_p and a shown for an ideal HAWT (Hansen, 2008).

It can be seen that the maximum C_p occurs at a equal to $1/3$. The value of C_p is 0.59 and C_T is 0.89 (Leishman, 2006). The theoretical maximum power output is known as the Betz limit (Hansen, 2008). This occurs at higher upstream wind speeds and thus higher values of a .

There are many weaknesses with the BEM method. It does not account for values of a larger than 0.4 because of the turbulent wake state. This problem is also present at smaller values of a , as a result of the pressure term from the rotation of the wake being discarded. This pressure term is less at the center of the wake and greater at the outside

of the wake. By not including this term, the BEM method overestimates the induction for low values of r/R and underestimates induction for large values of r/R .

This problem was addressed by Madsen, et al. (2007) with a numerical study of an actuator disk. They were able to pinpoint the physics that were causing these misrepresentations in the BEM method and suggested modifications that closely matched their results. The first problem was that the rotation of the wake was causing a slight resistance toward the hub of the rotor. To address this issue, they suggested adding an integral adjustment over the radius to the induced velocity ($V_0 - u$). The second problem was that the centrifugal forces in the rotating wake were causing a decreased induction toward the tip of the rotor. In response, Madsen, et al. (2007) similarly suggested subtracting an integral adjustment over the radius from the induced velocity. With both of these integral adjustments to the induced velocity, their study found very similar results between the numerical analysis of an actuator disk and the modified BEM method.

Modifications to the BEM method now allow for rotational, induction factor, and tip loss corrections (Hansen, 2008). These modifications make the BEM method an integration over the span of a blade. This is implemented in some codes, the most popular of which is the NREL AeroDyn code incorporated in FAST, the structural mechanics code published by NREL (Jonkman & Buhl Jr., 2005). The benefits of using BEM include rapid calculations, consideration of rotational wakes, increased induction factors, and tip loss corrections. BEM is also reasonably accurate for the modeling of wind speeds around the rated wind speed (Hansen, 2008).

The BEM method is a significantly simplified method for obtaining a theoretical maximum power extraction for a given wind scenario. BEM lacks the ability to model wake development and resolution downstream of the turbine and is not accurate for wind speeds at either end of the operational zone. Furthermore, BEM is only valid for a single tower model and it is difficult to model complex wind fields (Hansen, 2008; Jonkman & Buhl Jr., 2005). It is however, a simple and approximate method for estimating energy extraction.

2.2 ELEMENTARY WIND MODELS

There are many factors that affect power generation in wind turbines. Some of the more considerable ones are the wind speed, the equivalent density altitude, wind gusts, and the tower height. The tower height is important because wind velocity gradients can change substantially in the ABL. This velocity gradient is highly dependent on surface terrain conditions, much like pipe flow and open channel flow. However, in ABLs, stratification plays a significant role in velocity gradients and boundary layer formation. The reduced velocity at lower elevations also reduces the overall mass flow through the turbine, reducing the total power output and increasing the fatigue over the life of the turbine. These factors are very important for wind farm design and placement. Wind data is generally studied for years prior to implementation of a wind farm. This study includes the modeling of the boundary layer velocity gradients. Since it is prohibitive to study wind patterns at elevations as high as those of implemented turbines, measurements are generally performed at an elevation of ten meters. This data then needs to be extrapolated to the elevation of the potential wind turbines (Leishman, 2006). The most elementary models, as described by Leishman

(2006), for predicting the neutral boundary layer are the power law and the logarithmic law. It should be noted that these methods only produce reasonable predictions for perfectly neutral ABL flow.

The power law states:

$$V_{\infty}(h) = V_{\infty}(h_{ref}) \left(\frac{h}{h_{ref}} \right)^m, \quad \text{Equation 18}$$

where $V_{\infty}(h_{ref})$, is the known wind speed at a reference height, normally ten meters, h is the desired height above ground level, and m is a terrain related coefficient.

The logarithmic law states:

$$V_{\infty}(h) = V_{\infty}(h_{ref}) \left(\frac{\ln\left(\frac{h}{z_0}\right)}{\ln\left(\frac{h_{ref}}{z_0}\right)} \right), \quad \text{Equation 19}$$

where z_0 , is the roughness length. Both the power law and logarithmic laws are only valid for flat terrain. When topographical features are considered a full CFD model is necessary. Typical values for z_0 and m can be found in Table 1.

Table 1 Typical values of z_0 and m (Leishman, 2006).

Type of Terrain	z_0 (m)	m
Open country	0.02	0.12
Rural with few trees	0.05	0.16
Rural with trees and towns	0.3	0.928
Open water	0.001	0.01

Typical logarithmic velocity profiles can be seen in Figure 6. For this example, a velocity of 13.4 meters per second was used. The wind turbine pictured is modeled with 100-meter diameter blades and a hub height equal to 1.5 times the diameter (D) of the blades.

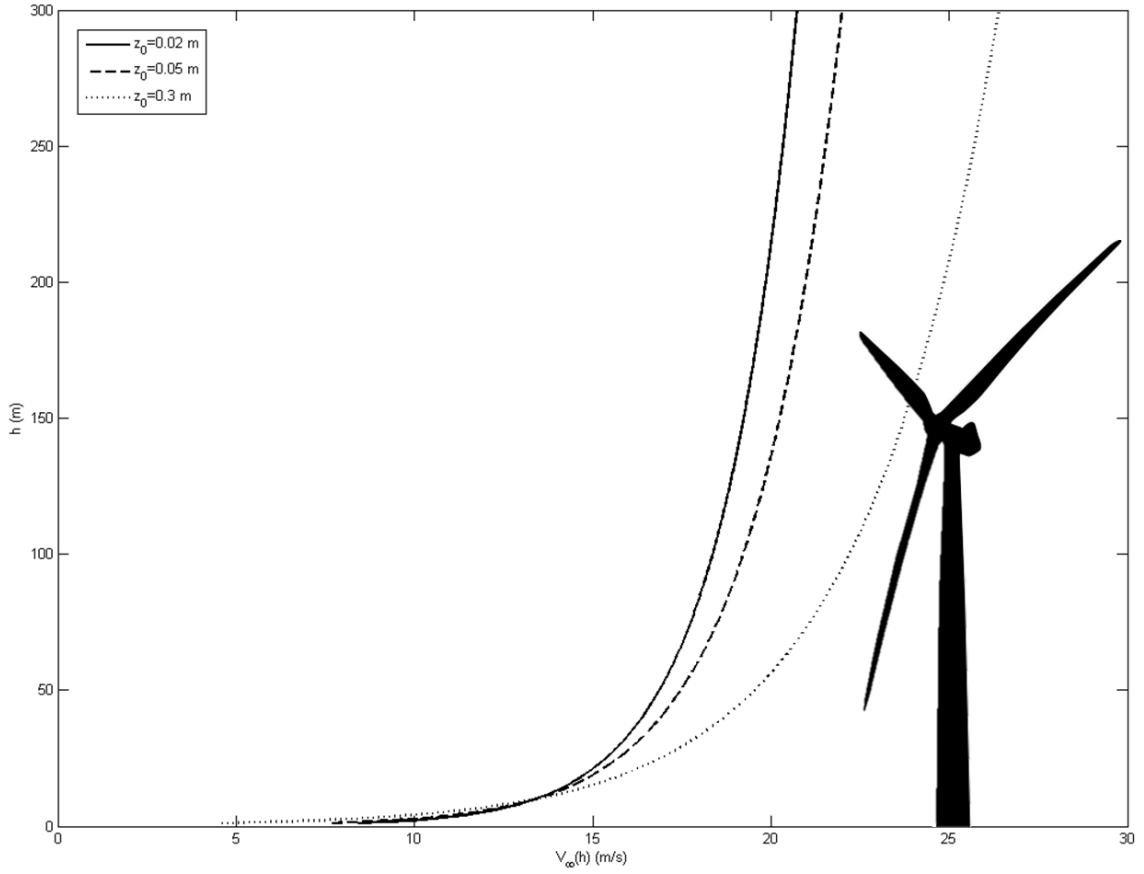


Figure 6 Logarithmic boundary layer velocity profiles for varying roughness coefficient, with a reference wind speed of 13.4 m/s.

Since the wind is rarely constant, stochastic variations as a result of turbulence must be considered since they affect the power output of the turbine. The velocity as a function of time can be represented by $V_{\infty}(t)$,

$$V_{\infty}(t) = \bar{U} + u(t), \quad \text{Equation 20}$$

where \bar{U} is the mean wind velocity and $u(t)$ represents the fluctuation in wind velocity at time t . This information is more commonly used as part of a turbulence intensity factor,

$$I_u = \frac{1}{\bar{U}} \left[\int_0^T u(t)^2 dt \right]^{1/2}, \quad \text{Equation 21}$$

where T is the total time $V_{\infty}(t)$ was measured, generally ten minutes. In practice, I_u ranges between $0.1\bar{U}$ and $0.2\bar{U}$, although it can be higher if the upstream terrain is rough. For design purposes it is important to note that as the height of the tower increases the turbulence intensity decreases. In addition the turbulence intensity factor is generally higher for lower wind speeds (Leishman, 2006).

For economic purposes it is important to also consider the proposed turbine's capacity factor. The turbine's average power can be represented by Equation 22,

$$\bar{P} = \int_0^{\infty} P(V_{\infty}) p(V_{\infty}) dV_{\infty}, \quad \text{Equation 22}$$

where $p(V_{\infty})$ is the probability of a wind velocity occurring and $P(V_{\infty})$ is the power that wind speed would generate. From this it can be said that the capacity factor is the ratio of average power to the rated power generation of the turbine. These values are generally less than 50% (Leishman, 2006).

Since these are the most elementary wind models, their predictions are far from exact. They have a tendency to under-predict structural loads in part because they only consider the velocity normal to the turbine. By leaving out the lateral and vertical aspects of velocity these models overlook the associated unsteady loads (Leishman, 2006).

A more advanced three-dimensional model is described by Hansen in his book *Aerodynamics of Wind Turbines*. This model uses a power spectral density function (PSD) to describe the wind velocity at one point, which is then coupled with a coherence function to get a time history for all desired points for a given $U(u, v, w)$ independently. Several different functions exist but for this example a Kaimal spectrum was used, defined as,

$$PSD(f) = \frac{I^2 V_{10min} l}{\left(1 + 1.5 \frac{f \cdot l}{V_{10min}}\right)^{5/3}}, \quad \text{Equation 23}$$

where the turbulence intensity, I , is the ratio of standard deviation of velocity fluctuations to the ten-minute average velocity. The frequency, f , is measured in hertz, and l is a length scale corresponding to $20h$ for h less than 30 meters and 600 for h greater than or equal to 30 meters. For N time steps the time-dependent velocity function can be written as,

$$u(t) = \bar{u} + \sum_{n=1}^{N/2} \sqrt{\frac{2PSD(f_n)}{T}} \cos(f_n t - \varphi_n), \quad \text{Equation 24}$$

where φ_n is the phase angle at frequency f_n . Since φ_n is not reflected in the PSD function it can be modeled by a random number generator with values between zero and 2π . Assuming a sample frequency of $f_s = \frac{1}{\Delta t}$, then the highest resolution that the discretization can detect is $f_h = \frac{N/2}{T}$, and the lowest resolution is $f_{low} = \frac{1}{T}$. The PSD function assumes a frequency range from zero to infinity, so it can be scaled to f_{low} and f_h as,

$$\int_{f=\frac{1}{T}}^{f=\frac{N/2}{T}} PSD(f) df = 1. \quad \text{Equation 25}$$

For 2 or more points in space, the time histories are not independent. The dependency is related to their distance apart and the frequency. Small frequencies can be attributed to small vortices and similarly large frequencies can be attributed to large vortices. Let L be the distance between points j and k . Coherence as a function of L and f can be expressed as,

$$\text{coh}_{jk}(L, f) = \exp\left(-12\left(\frac{fL}{V_{10min}}\right)\right). \quad \text{Equation 26}$$

The S_{jk} matrix can also be formed,

$$S_{jk} = \text{coh}_{jk} \sqrt{S_{jj} \cdot S_{kk}}, \quad \text{Equation 27}$$

where S_{jj} and S_{kk} are the PSD functions for j and k respectively. If NP is the number of points being evaluated then S_{jk} is a $NP \times NP$ matrix. Next a lower triangular matrix H is formed,

$$H_{11} = S_{11}^{1/2}, \quad \text{Equation 28}$$

$$H_{21} = \frac{S_{21}}{H_{11}}, \quad \text{Equation 29}$$

$$H_{22} = (S_{22} - H_{21}^2)^{1/2}, \quad \text{Equation 30}$$

$$H_{31} = \frac{S_{31}}{H_{11}}, \quad \text{Equation 31}$$

$$H_{jk} = (S_{jk} - \sum_{l=1}^{k-1} H_{jl}H_{kl}) / H_{kk}, \quad \text{Equation 32}$$

$$H_{kk} = \left(S_{kk} - \sum_{l=1}^{k-1} H_{kl}^2 \right)^{1/2}. \quad \text{Equation 33}$$

For each k , and discrete frequency $f_m = \frac{m}{T}$ there is a random φ_m between zero and 2π . Let m range between one and $N/2$ where N is the number of discrete points in time such that $t = i \cdot t$ for $i = 1, \dots, N$. There is a complex vector $V_j(f_m)$ described as,

$$\text{Re}(V_j(f_m)) = \sum_{k=1}^j H_{jk} \cos(\varphi_{km}), \quad \text{Equation 34}$$

$$Im(V_j(f_m)) = \sum_{k=1}^j H_{jk} \sin(\varphi_{km}). \quad \text{Equation 35}$$

V is then transformed in to an amplitude and phase,

$$Amp_j(f_m) = \sqrt{Re(V_j(f_m))^2 + Im(V_j(f_m))^2}, \quad \text{Equation 36}$$

$$\tan\varphi_j(f_m) = \frac{Im(V_j(f_m))}{Re(V_j(f_m))}. \quad \text{Equation 37}$$

The time history at points $j = 1, \dots, NP$ can now be written as,

$$U_j(t) = \bar{u} + \sum_{m=1}^{N/2} 2 Amp_j(f_m) \cos(2\pi f_m t - \varphi_j(f_m)). \quad \text{Equation 38}$$

This function gives a strong correlation for small values of f . Since it calculates the time history at all points for each $U(u, v, w)$ independently there is no guarantee of obtaining cross-correlation. A typical array of points where U is calculated is shown in Figure 7. Methods similar to the Power Spectral Density method described above are mostly applicable in codes similar to the AeroDyn module of FAST, for determining the aerodynamic loading of blades (Hansen, 2008). This method lacks the ability to recreate atmospheric phenomena and structures to determine subsequent interactions.

To recreate realistic atmospheric conditions, CFD solutions of the Navier-Stokes equations must be studied. A variety of complexities of studies exist in this field, from full LES simulations of diurnal planetary boundary layers (PBL) to two-equation (such as $k-\varepsilon$ model) RANS simulations of neutral ABL boundary conditions. A discussion of select CFD studies is provided in the following section.

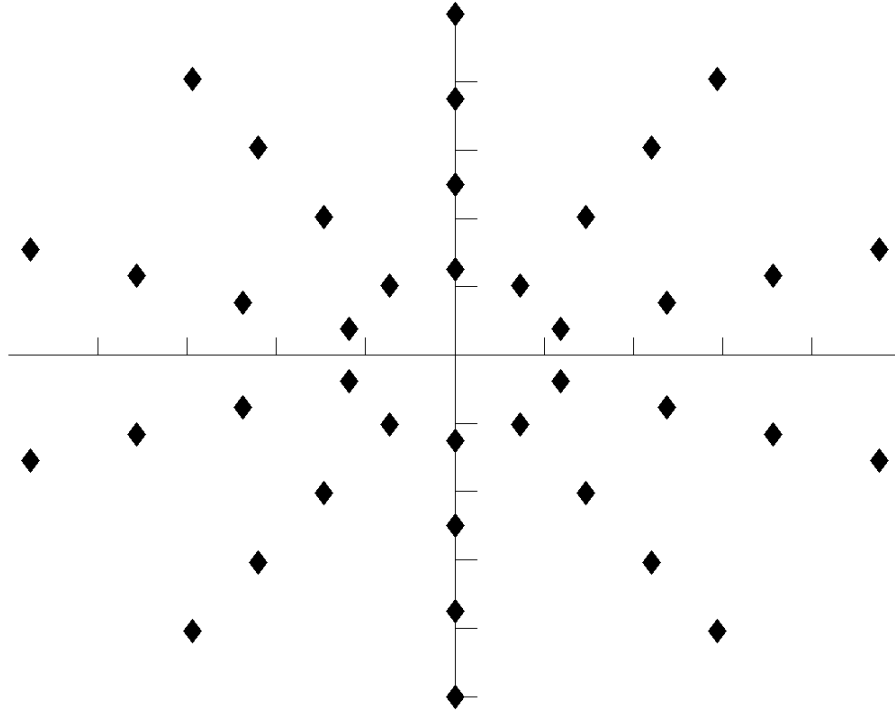


Figure 7 Points around a turbine where velocity history is typically calculated (Hansen, 2008).

The first study investigated here is that of O’Sullivan et al. (2011). The study includes boundary conditions and wall functions used in ABL modeling. The researchers used a classic neutral ABL. When using a $k-\varepsilon$ RANS turbulence model, frequently there are wall functions incorporated into the model to more accurately capture the near wall behavior (Menter, 1994). Many errors can be avoided by selecting a wall function that is consistent with the profile being investigated. Most importantly, the interior of the profile must be in equilibrium with the profile calculated by the wall function (O’Sullivan, et al., 2011). This issue of near wall behavior addressed by wall functions can be avoided by using a RANS model derived with wall bounded behavior in mind like the $k-\omega$ models (Menter, 2009).

It is a common practice to prescribe Neumann boundary conditions (e.g. zero-gradient fluxes) at the top of the boundary layer (O’Sullivan, et al., 2011). In ANSYS

FLUENT this type of boundary is called a symmetry boundary condition (ANSYS, 2010). This is most frequently done to minimize the size of the domain. In ABL flow, however, the top boundary condition should allow for fluids to exit and re-enter the domain to account for vertical flows induced by objects. By their nature zero-gradient boundary conditions prevent vertical flows across the boundary. O'Sullivan et al. (2011) solved this problem by setting a constant shear stress at the top boundary since the top boundary is sufficiently inside the constant shear stress layer. The gradients can thus be calculated. This approach has the advantage of the zero-gradient models with the gradients calculated from the inflow profiles allowing for flow to enter and exit the domain.

The results of O'Sullivan et al. (2011) show that the error associated with the proposed boundary conditions were of the same order as the convergence criteria, while the error associated with the zero-gradient boundary conditions caused the model to overestimate velocities up to four percent and underestimate turbulence intensities by as much as three percent. They also found that these errors held for models with much taller domains trying to account for the zero-gradient top boundaries.

Another example of the use of $k-\varepsilon$ RANS turbulence closure was performed by Montavon (1998). In this study, a finite volume commercial CFD code, FLOW-3D, was utilized to model neutral and stratified flows over complex terrain. To achieve a model capable of handling stratified flows the conservation equation and buoyancy term was implemented with potential temperature. Conditions of hydrostatic dominance and non-hydrostatic dominance were studied to determine the importance of vertical inertia. The first geometry studied was a 3-D domain containing a 2-D theoretical bell-shaped

mountain. The results were found to correlate closely to the solutions found using linear mountain wave theory. The last simulation performed was of the extreme wind event experienced in Boulder, Colorado in January 1972, where 60 mph winds were experienced. This model was initialized with measurements taken in Grand Junction, Colorado, 300 km upwind. The results compared respectably (Montavon, 1998).

The two previous RANS studies were successful in simulating fairly simple ABLs, however, the neutral ABL is a simplification of ABL conditions experienced with an assumed constant vertical density. To achieve more accurate ABL conditions, more sophisticated LES models must be used. Saiki et al. (2000) studied two very stable ABL cases using a LES model with a modified two SGS model. The cases investigated were a fanning or layering case prone to pollutants spreading out and a case with the forming of a nocturnal low-level jet (LLJ) (Saiki, et al., 2000).

In the case of the fanning or layering of very stable ABL, Saiki, et al., (2000) were unsuccessful, only obtaining a mildly stable ABL. They attribute this failure to the SGS turbulence model. As stability increases the dominant eddies become much smaller (Saiki, et al., 2000). This puts a considerable extra burden on the SGS model (Basu, et al., 2008). To reasonably predict the strongly stable ABL, significant advances in SGS models need to be made (Saiki, et al., 2000).

In the case of the nocturnal LLJ, Saiki et al. (2000) were successful in recreating a previously established event (Blackadar, 1957). The study had reasonably well-correlated surface mean velocity and temperature profiles for the nocturnal LLJ.

The modeling of convective and neutral ABLs has reached its maturity. However, the modeling of stable ABL is still a field on the cutting edge with only a

handful of successful studies (Basu, et al., 2008). The LES study by Basu et al. (2008) used a locally averaged scale-dependent dynamic (LASDD) SGS model to describe a full diurnal ABL cycle. One of the current drawbacks of LES is its dependence on the SGS model to capture the effect of the small scale eddies that are not resolved. Since eddies become increasingly small in stable conditions, a lot of burden rests on the SGS model to account for these smaller eddies. By using the tuning-free (dynamically computed) LASDD SGS model, Basu et al. (2008) were able to better account for the SGS eddies. Other complications that arise when modeling both convective and stable ABLs are the domain size and grid size. To properly capture the convective ABL, a large domain is needed. However, for a stable ABL, fine grid resolution is required. This leads to a mesh size of the order 10^9 and an exceedingly small time step requiring massive computing power.

The objective of the study by Basu et al. (2008) was to determine if the LASDD SGS model was capable of modeling diurnal cycles inclusive of strongly stratified ABLs. To test this, they simulated day 33 and night 33/34 of the Wangara case study. The Wangara case study was performed in Hay, Australia in 1967. The location was a flat vegetation free area to reduce any topographical effects (Clarke, et al., 1971). The simulation run by Basu et al. (2008) was able to qualitatively reproduce the diurnal ABL cycle including the formation of a nocturnal LLJ in magnitude, direction and duration. However, the elevation of the LLJ was shallower than the one experienced in the Wangara experiment showing that the shear layer was under estimated. This under-prediction could be very critical when designing wind farms as a predicted shallow nocturnal LLJ could significantly impact a wind farm. As was found in earlier studies,

Basu et al. (2008) also found that, the mixed layer temperature was slightly lower than the actual temperature experienced. However, it should be noted that radiant surface heating was not included in the model.

As a means to show the extent of modeling required, Sullivan & Patton (2011) performed a grid independence study. In this study they modeled a weakly sheared convective PBL through a set domain size in open terrain while varying the grid size. The grid sizes used were 32^3 , 64^3 , 128^3 , 256^3 , 512^3 , and 1024^3 . This study was run on as many as 16,384 processors. They found that there was some convergence at a resolution of 256^3 . However, vertical temperature fluxes did not fully converge for any of the grid resolutions. This study clearly shows the extent of modeling required to accurately resolve even a relatively simple atmospheric condition.

2.3 POWER CURVES

Predicting the power output of a wind turbine as a function of wind speed is very important. This is accomplished by developing specific power curves for each different wind turbine model. In these wind models there is a cut-in wind speed, in which any wind below the cut-in velocity does not create any power output. This is because of mechanical friction and aerodynamic losses that must be overcome before power can be generated. Variable pitch turbines start with high angles of attack so some stall is present. In addition, turbines start in a turbulent wake state so there are additional losses that must be overcome by a higher wind velocity prior to power generation. From the cut-in wind speed the power output rapidly increases and is proportional to V_{∞}^3 as shown in Equation 39 (Leishman, 2006).

$$P = \frac{1}{2} \rho A |V_{\infty}|^3. \quad \text{Equation 39}$$

As the power approaches the rated power, it is necessary to implement controls to prevent the generator from absorbing more power than it is capable. This limitation is accomplished most frequently with blade pitch control by putting the turbine into a semi-stalled state to match the desired power output (Leishman, 2006).

Power curves can be represented in many ways as long as they show the relation between power and wind speed. One of the more common ways to represent a power curve is as a relation between the power coefficient and the tip-speed ratio. Where the tip-speed ratio X_{TSR} is,

$$X_{TSR} = \frac{\text{turbine tip speed}}{\text{wind speed}} = \frac{\Omega R}{V}. \quad \text{Equation 40}$$

For most large scale, fixed tip speed turbines, the maximum efficiency is 85 percent. This maximum efficiency only occurs for a very narrow range of wind speeds. Variable speed turbines can have a larger region of efficiency in lower wind speeds, however, the efficiency drops much faster than fixed speed turbines in high winds (Leishman, 2006). This is illustrated in Figure 8. Figure 9 shows the power curve for the NREL 5MW reference turbine used in this thesis work.

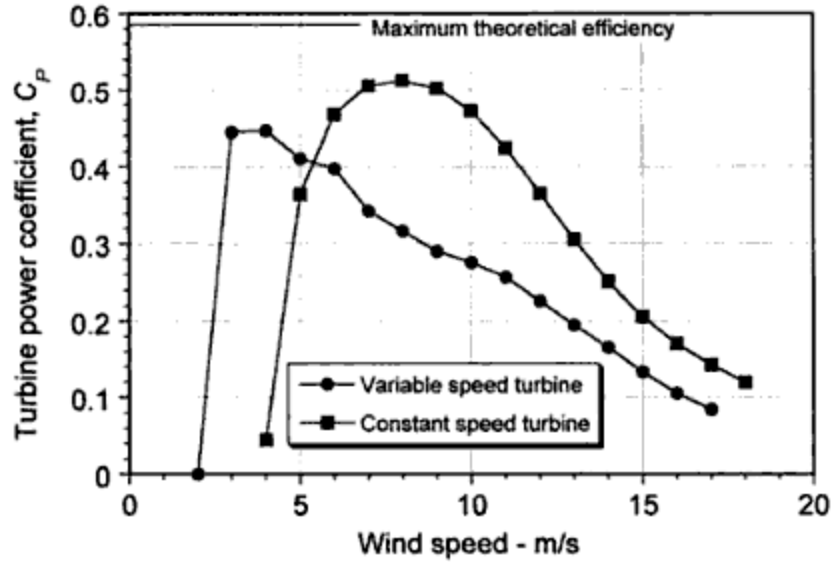


Figure 8 Representative power coefficient versus wind speed curves for constant speed and variable speed HAWTs (Leishman, 2006).

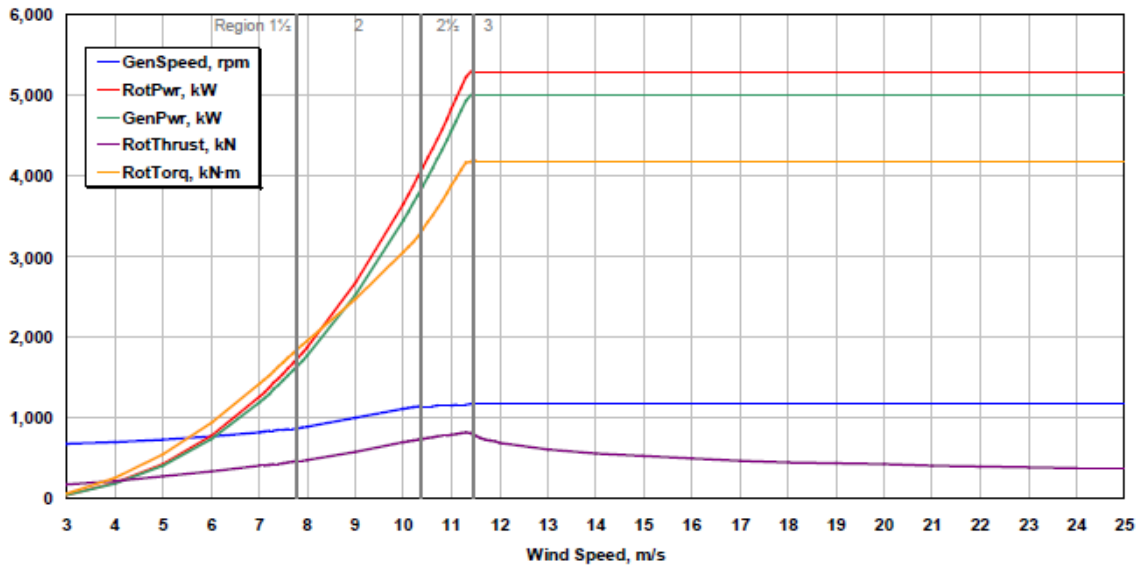


Figure 9 Power Curve for NREL 5MW reference turbine (Jonkman, et al., 2009).

A dynamic power curve has been proposed by Gottschall & Pienke (2007). Rather than basing the power curve off of a ten-minute average wind speed like the International Electrotechnical Commission (IEC) code suggests, they split the wind speed into an average and a stochastic wind speed, much like the Reynolds decomposition

widely used in turbulent flows. This allowed them to look at small time scale dynamics of power generation. Their dynamic formula to calculate power is:

$$\frac{d}{dt}P(t) = D^{(1)}(P; u) + \sqrt{D^{(2)}(P; u)}\Gamma(t), \quad \text{Equation 41}$$

where $D^{(1)}(P; u)$ is the drift coefficient responsible for the average wind speed part of the equation, $D^{(2)}(P; u)$ is the diffusion coefficient which, when combined with the Langevin force, $\Gamma(t)$, is responsible for the stochastic aspect (Gottschall & Peinke, 2007). Figure 2 compares the exact power curve, the IEC power curve and Gottschall & Peinke (2007) dynamic power curve.

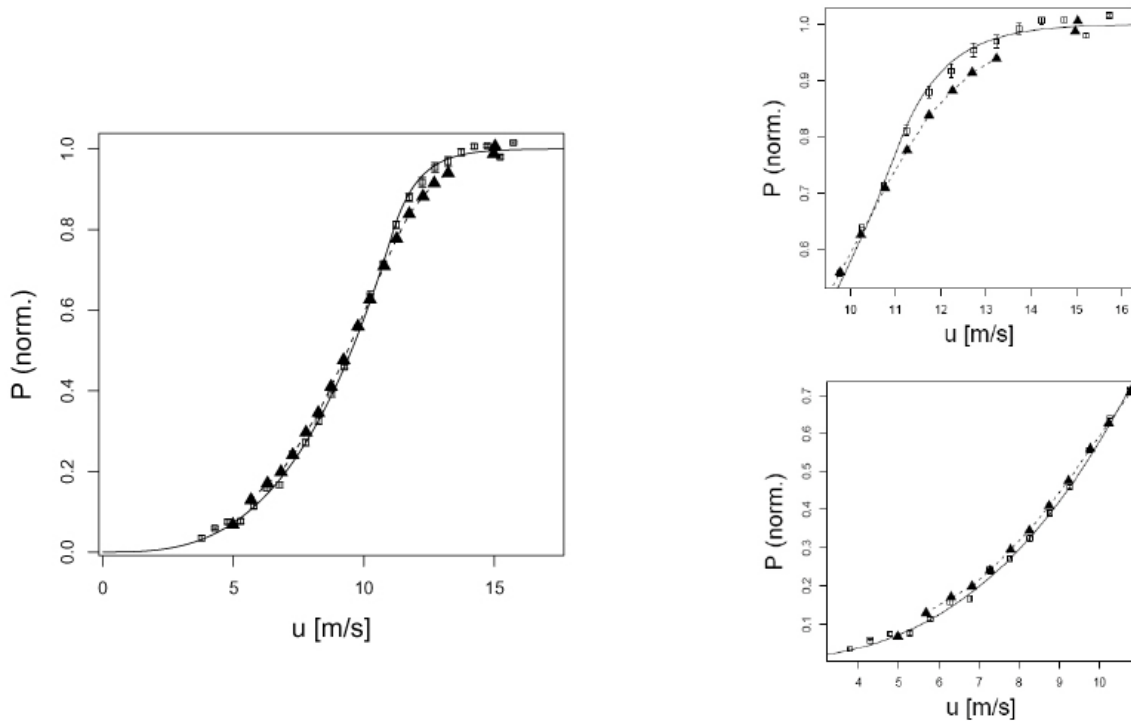


Figure 10 Comparison of power curves. Exact (solid line). IEC (filled triangles). Dynamic (open squares with error bars) (Gottschall & Peinke, 2007).

Gottschall & Peinke (2007) conclude that their dynamic power curve cannot replace the IEC standard curve but is simply another way to look at power characteristics.

Power curves do not play a large role in CFD studies of wind turbines, but they can provide important information when designing and analyzing wind turbines.

2.4 CFD WIND TURBINE MODELS

Empirical models, like the BEM method, have played an important role in the development of the wind energy industry. However, as the industry continues to grow and prime farm sites become scarcer, resulting in higher density turbine placement, advanced CFD simulations will be required to meet demand and advance the industry (Bazilevs, et al., 2010). A variety of techniques and methods have been used to study wind turbine wake interactions (Fletcher & Brown, 2010; Hahm & Wußow, 2006; Porté-Agel, et al., 2011; Tachos, et al., 2010), atmospheric wind farm effects (Calaf, et al., 2010; Meyers & Meneveau, 2011), and structural loads and spacing (Bazilevs, et al., 2010; Meyers & Meneveau, 2011). These studies range from using RANS turbulence closures (Hahm & Wußow, 2006; Tachos, et al., 2010), to LES with a variety of SGS models (Bazilevs, et al., 2010; Calaf, et al., 2010; Meyers & Meneveau, 2011; Porté-Agel, et al., 2011), to a case using the vorticity transport model (VTM) (Fletcher & Brown, 2010). The following Literature review will explore their studies and what can be learned from their methods and results.

The effect of land scarcity in Germany with turbines spaced as close as $3D$ has spurred increased regulation with respect to turbine fatigue (Hahm & Wußow, 2006). This increased regulation is based in rudimentary empirical calculations of turbulence intensity. A study by Hahm & Wußow (2006) investigated the structure of turbulence intensity comparing their results to common empirical methods. Their study focused on the wake structure behind a single MW class turbine using both $k-\varepsilon$ RANS model and a

detached eddy simulation (DES) model. The empirical model investigated casts the turbulence intensity in the far wake as the sum of the upstream turbulence intensity and a bell-shaped turbulence intensity defined as a function of thrust coefficient and the tip-speed ratio. The results of their study gave an idealized modification to the empirical model by casting the additional turbulence intensity as three bell-shaped curves with the primary peaks aligned with the tip vortices (Hahm & Wußow, 2006). A comparison of the two models is provided in Figure 11.

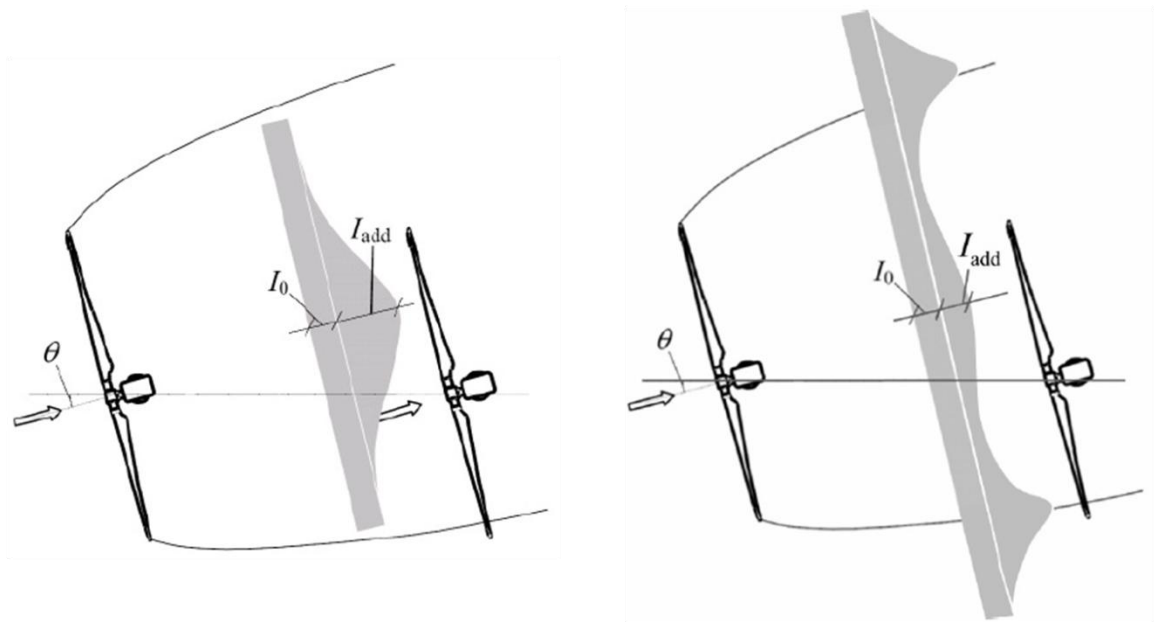


Figure 11 Distribution of turbulence intensity in wake for empirical model (left), and idealized results of CFD study (right) (Hahm & Wußow, 2006).

The $k-\varepsilon$ RANS study simulated a previously studied 55kW turbine with a neutral ABL using a multiple reference frame model in FLUENT. Results were relatively successful at reproducing velocity profiles measurements downstream, yet due to the averaging nature of RANS models the turbulence intensities near the edges of the wake were under-predicted (Hahm & Wußow, 2006).

The DES simulation used a homogeneous ABL to model an ENERCON E66 turbine for which turbulence data was available. This model also produced relatively successful results. The error in the DES model was attributed to boundary influences from a limited domain size. This resulted in an under-prediction of turbulence intensity just outside the wake region (Hahm & Wußow, 2006).

Although Hahm & Wußow (2006) experienced some difficulties with the $k\text{-}\varepsilon$ RANS closure model, other RANS closure models should be explored. Tachos et al. (2010) performed a parametric study of RANS closure models on the NREL Phase II wind turbine to determine the applicability of RANS closure models. The models used include Spalart-Allmaras (SA), $k\text{-}\varepsilon$, $k\text{-}\varepsilon$ renormalization group (RNG), and the $k\text{-}\omega$ shear-stress transport (SST) closure models. The simulation was set up using a single blade from the NREL Phase II turbine in a single reference frame with 120° periodic boundary conditions. As a perspective of the size and computation time, the mesh was 4.2 million cells and the $k\text{-}\omega$ SST model took the equivalent of 20 days of central processing unit (CPU) time. The model was run as steady state in FLUENT. The means of validation used by Tachos et al. (2010) was pressure distribution on the blade surfaces. They found that the $k\text{-}\omega$ SST model had a very good correlation with measured values. The $k\text{-}\varepsilon$ RNG and SA models had fairly good correlation. The discorrelations found were determined to be a result of flow separation. The $k\text{-}\varepsilon$ closure model performed very poorly, likely as a result of its lack of an explicit term to account for rotation. Overall it was concluded that because of the near wall formulation, the $k\text{-}\omega$ SST model was the most suited RANS turbulence closure model for wind turbine simulations.

Although RANS simulations can achieve accurate and meaningful results they only calculate the mean flow and parameterize the scales of turbulence (Porté-Agel, et al., 2011). For more accurate and descriptive results LES simulations are required. LES models use a filter based on grid size so that where the mesh is fine enough the flow is resolved, similar to direct numerical simulation (DNS), and where the mesh size is too coarse, a SGS turbulence closure scheme is used to model the flow. The objective is to have a grid size small enough to resolve 80% of the energy (Pope, 2010). This places a large restriction on the grid size of LES models.

Porté-Agel et al. (2011) performed a LES study using a tuning-free Lagrangian dynamic SGS model recently developed for wind energy applications to model both single turbine wakes and wake interactions in an operating wind farm. Fully resolving a rotating wind turbine significantly increases CPU time and model complexity. As a means of simplifying the model and cost savings, an actuator disk model (ADM) can be implemented to act as a momentum sink with properties mirroring that of a wind turbine. Porté-Agel et al. (2011) studied three different actuator disk models. The first was a non-rotating actuator disk model (ADM-NR). For this model the Rankine-Fronde actuator disk model was used for its widely accepted ability when using coarse grids. This model assumes that forces only act in the axial direction eliminating the ability for the model to capture rotation. For the ADM-NR, the force, F_x , is represented as,

$$F_x = \frac{1}{2} \rho \tilde{u}_0^2 A C_T, \quad \text{Equation 42}$$

where \tilde{u}_0 is the unperturbed resolved velocity of axial incident flow acting on the center of the disk, A is the swept area of the rotor, and C_T is the thrust coefficient. The second model used was a rotating actuator disk model (ADM-R). This model uses the BEM

method described in section 2.1, integrated over the rotor disk to calculate 2-D forces. This results in the ability of the ADM-R to model rotation. However, because it is integrated over the area of the disk, it is not able to capture the tip vortices. The final model studied was an actuator line model (ALM). This model uses the BEM method to calculate turbine induced lift and drag forces, and evenly distributes them along the actuator lines. By using lines rather than a disk, the ALM is capable of capturing tip vortices and uses far fewer cells than resolving the actual turbine blades. The main advantage of using the actuator models is a reduced mesh size and subsequently reduced computational costs.

The actuator models were validated against a wind tunnel experiment Porté-Agel et al. (2011) performed using a 0.15 meter diameter wind turbine model and a log-law incident neutral ABL. As can be seen in Figure 12, the ADM-R and ALM models very closely align with the measurement in the near and far wake regions. The ADM-NR model underestimates the velocity deficit in the near-wake region but agrees quite well in the far wake region. The results of turbulence intensity were not as close. The ADM-R and ALM models both correlated very well with each other but only correlated reasonably well with the wind tunnel data. The ADM-NR on the other hand under-predicted the turbulent intensity across the board.

The operational wind farm Porté-Agel et al. (2011) chose for this study is located in Mower County, Minnesota. Five turbines located in an outlying section upwind of the main farm were chosen. Measurements were made using a technique called sonic detection and ranging (SODAR). SODAR measures the vertical wind profiles using three beams offset 10° from vertical. Two SODAR instruments were utilized. One was

placed in line with the first row of turbines. The second was placed about halfway between the first and second in-line turbines. Measurements were taken during a time when a fairly neutral ABL was present. As a result, Coriolis and buoyancy were neglected in the CFD model. Once again very strong agreement was found between the measured velocity field and the ADM-R and ALM results behind the first turbine. Similar to the previous case, the ADM-NR under-predicted the velocity deficit behind the first turbine. Turbulence intensities were under-predicted across the board by 20%. Since no other SODARs were used, subsequent wake interactions could not be compared (Porté-Agel, et al., 2011).

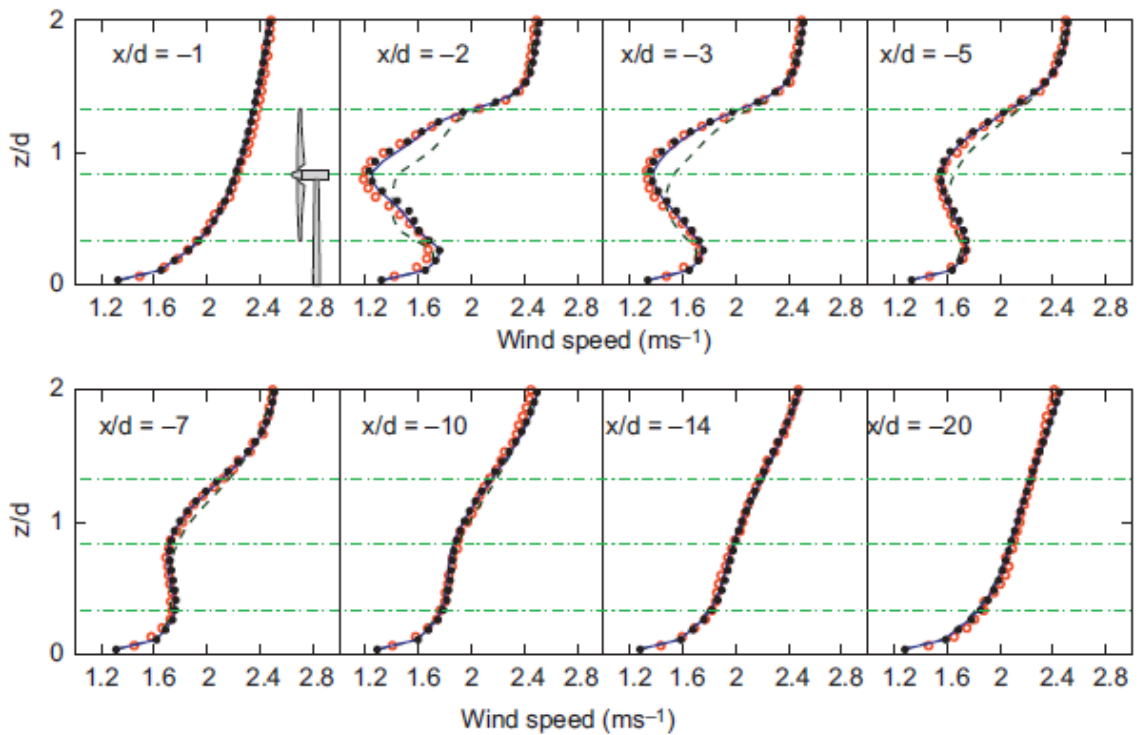


Figure 12 Streamwise velocity profiles (m/s): wind tunnel measurements (\circ), ADM-NR (dashed line), ADM-R (solid line), ALM (dotted line) (Porté-Agel, et al., 2011).

Power deficits seen by the second turbine were also compared. It was noted that the actual power deficits experienced in the wind farm by the second turbine were

between 47% and 50%. The ADM-R and ALM simulations both resulted in a power reduction of 48% whereas the ADM-NR simulation only resulted in a 37% power reduction. This was expected since the ADM-NR simulation significantly under-predicted the velocity deficit, as well (Porté-Agel, et al., 2011).

As wind farms continue to grow in size it is conceivable that they may start to affect the ABL in a similar manner to heavy vegetation. Although this does not have much potential to significantly affect the larger PBL, it could have a significant effect on wind farm production (Calaf, et al., 2010).

Calaf et al. (2010) proposed that wind farm arrays exceeding 10-20 km in size approach the infinite wind farm asymptotic limit, causing the boundary layer flow to be almost in a fully-developed state. There are several models that have been developed for atmospheric studies to predict the modified ABL as a function of surface roughness, z_0 . A comparison of two of these models, Lettau (1969) and Frandsen et al. (2006), was performed and a modification to the Frandsen formula was recommended. For their study, Calaf et al. (2010) developed a parametric study of wind farms using a LES model with a Smagorinsky SGS closure scheme. They modeled entire farms varying the number of turbines and spacing of those turbines. The setup of the study included modeling the turbines as non-rotating actuator disks, and using a pressure forced neutral ABL (Calaf, et al., 2010).

Calaf et al. (2010) noted that in wind tunnel experiments performed by Frandsen et al. (2006) in which streamwise spacings of 7.85 and larger were used, significant velocity recovery occurred prior to the subsequent turbine. This was reflected in the results of the CFD study performed by Calaf et al. (2010), as well. It has been observed

that when modeling single turbines, the energy comes from the difference in kinetic energy flux over the turbine. For an array of turbines the kinetic energy must be entrained from above. This is seen as a result of the vertical kinetic energy fluxes being of the same order of magnitude as the power extracted (Frandsen, et al., 2006). It was also observed that the turbine spacing only contributed about 10% to the total power production and effective roughness length. It was concluded that velocity changes in the streamwise direction can be neglected, since relevant exchanges of energy occur as a result of vertical entrainment (Calaf, et al., 2010).

Subsequent modifications were made to the Frandsen et al. (2006) ABL formulation to provide reasonable agreement with the CFD results. It was noted that a model resolving rotating blades would provide more accurate results. Due to computational restrictions this had to be avoided (Calaf, et al., 2010; Meyers & Meneveau, 2011).

Meyers & Meneveau (2011) built upon the study by Calaf et al. (2010) to develop formulas for the optimum turbine spacing. The study considered projected power production found as a result of Calaf et al. (2010) study, turbine cost ($cost_T$), and land acquisition cost ($cost_{Land}$). The formulation defined a ratio α , as:

$$\alpha = \frac{cost_T/A}{cost_{Land}}. \quad \text{Equation 43}$$

Here A , the swept area of a the turbine, was included to non-dimensionalize α . Several values of α were explored. It was found that for a value of $\alpha = 1$ the optimal spacing was $4D$. However for larger values of α , $10^3 < \alpha < 10^4$, that correlate better with low land prices found for offshore sites, the optimum turbine spacing was found to exceed $15D$ (Meyers & Meneveau, 2011).

Since many wind farms are spaced much closer than the formulated optimum spacing, Meyer & Meneveau (2011) investigated efficiency as well. It was found that if an efficiency of 95% was deemed acceptable the turbine spacing could be significantly reduced. For example, for an efficiency of 95% and an $\alpha = 10^4$, the recommended spacing of $25D$ could be reduced to $15D$. As a reference, the Horns Rev offshore wind farm was cited as having a spacing of $7D$ between staggered turbines. This could be very close to the optimum $15D$ spacing, but staggering was not investigated in this study (Meyers & Meneveau, 2011).

Wind turbine wake interactions are only the first half of the problem of understanding fatigue impacts on wind turbines, the second half of the problem is understanding the structural response to those fatigue loads. In a two-part study, the complete problem was studied using a LES model with a residual-based variational multiscale (RBVMS) formulation of the Navier-Stokes equations coupled with a linear elastostatic structural finite element method (FEM) model (Bazilevs, et al., 2010; Bazilevs, et al., 2011). For this simulation a full two-way coupling was established such that the deformation of the blades subsequently deformed the fluid domain at each time step allowing for a much more accurate capture of the fluid-structure interaction (FSI).

Validation for their fluid model was performed as a simulation of a Taylor-Couette flow. This flow consists of two concentric cylinders with the outer cylinder stationary and the inner cylinder rotating. The problem captures elements of rotation, curved walls, boundary layer, and time-dependent evolution of velocity pressure fields. Results are compared to a DNS simulation for a Reynolds number of 8000, computed with 256 Fourier modes. Bazilevs et al. (2010) note that this only constitutes a partial

validation of their model. To test their models, both a linear FEM and quadratic non-uniform rational B-splines (NURBS) solutions were calculated with constant grid size so the boundary was not resolved. Their results showed very close agreement of both models with the DNS data for the near wall region, with the boundary layer contained in the first cell. The NURBS solution was in much closer agreement through the middle region. However, the FEM solution did agree reasonably well.

When modeling the turbine, the domain was split into 120° symmetries, with periodic boundary conditions, so that only one blade was modeled. The NREL 5MW reference turbine was modeled with a uniform 9 m/s flow field. The turbine was set to rotate at a constant 1.08 rad/s. Using the cord length at $\frac{3}{4}R$ and the associated relative velocity, the Reynolds number was approximated at about 12 million. For this simulation a very close correlation was found between the FEM solution and the NURBS solution. The maximum pressure on the blade was found to be approximately 1.2 kPa (this will be discussed further with respect to the current thesis work in Chapter 4) (Bazilevs, et al., 2010).

A follow-up model was run to simulate turbine control mechanisms failing under a much higher incident flow field. The inlet velocity was set to 12 m/s and the turbine was allowed to spin freely. After one second it had reached an angular velocity of 3 rad/s at which point the simulation was stopped. The results of the study showed an under-prediction of torque as a result of flow separation in the poorly defined boundary layer; no grid independence study was performed.

Throughout the aforementioned studies many different RANS and LES formulations have been used, Fletcher & Brown (2010) used a vorticity transport model

(VTM) to study wake interaction between two in-line and offset NREL Phase VI turbines. The VTM method was originally developed by Brown (2000) and expanded by Brown & Line (2005). It was designed for analysis of helicopter rotors and flow with large Reynolds numbers, so an assumption of inviscid and incompressible flow is made to convert the Navier-Stokes equations into a vorticity-velocity form (Brown & Line, 2005). By using the VTM method, numerical dissipation experienced with the pressure-velocity-density solution of the Navier-Stokes equations can be avoided (Fletcher & Brown, 2010).

In the study performed by Fletcher & Brown (2010), the wake influence of in-line turbines with spacings varying between $2D$ and $8D$ were studied. They also studied turbines offset by $0.5D$ and $1D$ with an axial spacing of $2D$. No ABL was used and the ground was not included in the study. To model the turbines, a BEM formulation of actuator lines was implemented. They found that even with spacings of $6D$, power losses of 40% to 50% were still experienced. They also found that oscillations in the power coefficient increased as the spacing between turbines increased due to the wake structure and dissipation (Fletcher & Brown, 2010).

2.5 SUMMARIZING REMARKS

As these case studies illustrate, there are many different numerical solutions to the Navier-Stokes equations that have been implemented successfully. Of the RANS closure models, the $k-\omega$ SST model was seen to have the most success. With respect to LES, the tuning-free SGS models were the most widely used. However, LES requires a very fine grid resolution to not over burden the SGS model. A method to mitigate large mesh sizes is the widely used actuator disk model. A variety of ADMs exist, but the best results

were found among those formulated using the BEM method over a disk or actuator lines. To understand the larger picture of wake interactions and power losses, the entire wind farm must be modeled, however much is lost in the specific interaction of individual turbines. The interaction of just two turbines must be modeled for this purpose.

CFD modeling has come a long way in the past couple decades and has made great progress in the field of wind energy. In the most ideal simulation, the entire farm of fully resolved, rotating turbines would be modeled with a very fine grid, and the solution would be achieved using LES with a tuning-free SGS model. However, computational capabilities have not achieved a level able to handle this problem and as a result, simplifications to the models must usually be made. Some wake structures and rotational effects were not captured in ADM studies even with LES grid resolutions. To capture the rotating effects of the wake, it is may be better to use a coarser RANS simulation that fully resolves the rotating turbine, than to use a finer ADM LES simulation. The current thesis work is directed toward addressing this hypothesis.

CHAPTER 3. PARAMETRIC STUDY

The research discussion which follows explores the velocity deficit effect created by turbine wakes through a suite of RANS models in ANSYS FLUENT for a row of two in-line wind turbines. A parametric study of turbulence models was performed on two base geometries. The first geometry was a set of two in-line stationary NREL 5MW reference turbines (Jonkman, et al., 2009) spaced αD apart, where D is the diameter of the swept area, and α is the set of integers 5, 10, and 15 as seen in Figure 13. The second geometry was a set of two in-line non-porous disks, with the same diameter as the NREL 5MW reference turbine, spaced αD apart.

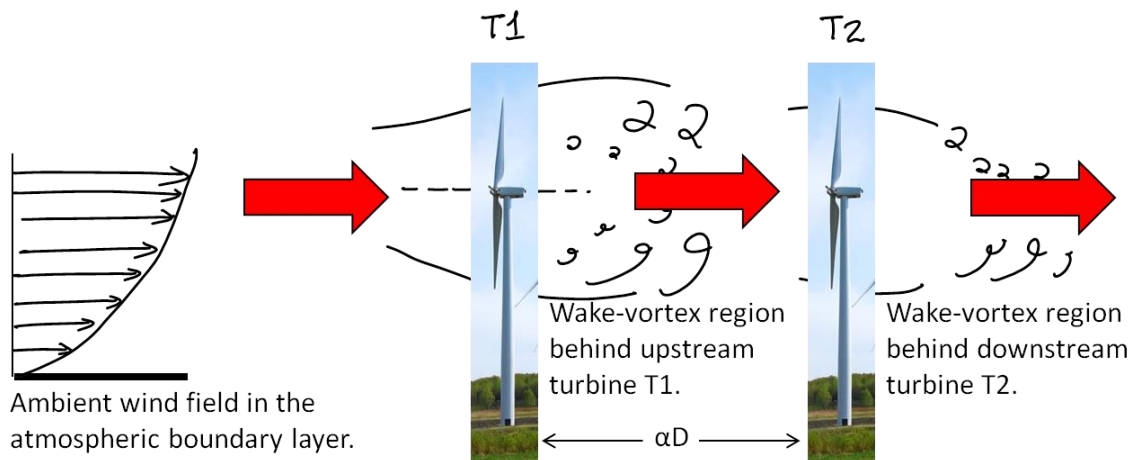


Figure 13 Schematic showing a one-dimensional array of two horizontal axis wind turbines.

The objective of this study was to understand the relative strengths and differences of the various turbulence models for separating flows while bounding the flow characteristics of a rotating NREL 5MW reference turbine. Determining the behavior of these turbulence models for simplified turbine scenarios allows for a more

educated selection of turbulence model when moving to a more sophisticated model (i.e. high resolution rotating model). All models were run on a four parallel processor system to demonstrate the capabilities of RANS models on non-supercomputer systems.

In the following sections, a brief theoretical overview of the numerical methods and models is provided in 3.1. The geometry, mesh and FLUENT pre-processing are described in 3.2. The results of the parametric study are discussed in 3.3.

3.1 THEORY

The theoretical basis for the problems of interest evolves from the conservations of mass (Equation 44) and momentum (Equation 45), represented by Pope (2010) as:

$$\frac{\partial \rho}{\partial t} + \nabla \cdot (\rho \mathbf{U}) = 0, \quad \text{Equation 44}$$

$$\rho \frac{DU_j}{Dt} = \frac{\partial \tau_{ij}}{\partial x_i} - \rho \frac{\partial \Psi}{\partial x_j}, \quad \text{Equation 45}$$

where, \mathbf{U} is the three-dimensional velocity vector, τ_{ij} is the stress tensor, and Ψ is the external body force vector (in this case the gravitational potential). Nonlinearities prevent the direct numerical solution to these Navier-Stokes equations and indicate the use of the assumption of the turbulent viscosity theory. These instantaneous momentum and continuity equations can be written in an averaged form with the substitution of the Reynolds decomposition as,

$$\mathbf{U}(\mathbf{x}, t) = \langle \mathbf{U}(\mathbf{x}, t) \rangle + \mathbf{u}(\mathbf{x}, t), \quad \text{Equation 46}$$

where, the \mathbf{x} vector represents the streamwise x direction, the spanwise y direction, and the vertical z direction (Pope, 2010). The stress tensor is represented by Equation 47:

$$\tau_{ij} = -P\delta_{ij} + \mu \left(\frac{\partial U_i}{\partial x_j} + \frac{\partial U_j}{\partial x_i} \right), \quad \text{Equation 47}$$

where P is the pressure, δ_{ij} is the Kronecker delta, and μ is the molecular viscosity (Pope, 2010).

The Reynolds decomposition substitution of Equation 46 into Equation 44 and Equation 45, however, creates the Reynolds stresses which present more unknowns than equations manifesting in a closure problem. To achieve this closure, a turbulence model is used. The majority of turbulence models are based on the turbulent-viscosity hypothesis. The Reynolds stresses can be represented by Equation 48:

$$\langle u_i u_j \rangle = \frac{2}{3} k \delta_{ij} - \nu_T \left(\frac{\partial \langle U_i \rangle}{\partial x_j} + \frac{\partial \langle U_j \rangle}{\partial x_i} \right), \quad \text{Equation 48}$$

where ν_T is the turbulent viscosity. Given the turbulent viscosity and an assumption for k , the turbulent kinetic energy closure can be achieved (Pope, 2010). The turbulent viscosity is gained through a turbulence model consisting of additional algebraic (zero-equation models) or partial differential equations (PDE) as described in the following subsections.

3.1.1 SPALART-ALLMARAS MODEL

Spalart-Allmaras is a one-equation turbulence model originally designed for the aerospace industry and made significant improvements over previous one-equation models (ANSYS, 2010). While being simpler and computationally less expensive, one-equation models lack the flexibility of higher equation models (Pope, 2010). Equation 49 shows the Spalart-Allmaras transport equation:

$$\begin{aligned} & \frac{\partial}{\partial t} (\rho \nu_T) + \frac{\partial}{\partial x_i} (\rho \nu_T u_i) \\ & = G_\nu + \frac{1}{\sigma_{\nu_T}} \left[\frac{\partial}{\partial x_j} \left\{ (\mu + \rho \nu_T) \frac{\partial \nu_T}{\partial x_j} \right\} + C_{b2} \rho \left(\frac{\partial \nu_T}{\partial x_j} \right)^2 \right] - Y_\nu + S_{\nu_T}, \end{aligned} \quad \text{Equation 49}$$

where G_ν and Y_ν are the production and destruction of turbulent viscosity, respectively, in the near wall regions as a result of wall blocking and viscous damping. σ_{ν_T} and C_{b2} are constants. ν is the molecular kinematic viscosity, and S_{ν_T} is a user-defined source term (ANSYS, 2010). It should be noted that at the wall the turbulent viscosity is set to zero and the shear stress is calculated by the laminar stress-strain relationship or the law-of-the-wall depending on grid size (ANSYS, 2010).

3.1.2 STANDARD k - ε MODEL

The k - ε turbulence model is named for the two quantities that are being solved, the turbulent kinetic energy k and the turbulent dissipation rate ε (Jones & Launder, 1972). It is classified as a two-equation model to reflect the two additional PDEs that are required to solve for the turbulent viscosity. It is the most common turbulence model in use (Pope, 2010). The transport equations as represented in ANSYS FLUENT are:

$$\frac{\partial}{\partial t}(\rho k) + \frac{\partial}{\partial x_i}(\rho k u_i) = \frac{\partial}{\partial x_j} \rho \left[\left(\nu + \frac{\nu_T}{\sigma_k} \right) \frac{\partial k}{\partial x_j} \right] + G_k + G_b - \rho \varepsilon - Y_M + S_k, \quad \text{Equation 50}$$

$$\begin{aligned} \frac{\partial}{\partial t}(\rho \varepsilon) + \frac{\partial}{\partial x_i}(\rho \varepsilon u_i) \\ = \frac{\partial}{\partial x_j} \rho \left[\left(\nu + \frac{\nu_T}{\sigma_\varepsilon} \right) \frac{\partial \varepsilon}{\partial x_j} \right] + C_{1\varepsilon} \frac{\varepsilon}{k} (G_k + C_{3\varepsilon} G_b) - C_{2\varepsilon} \rho \frac{\varepsilon^2}{k} + S_\varepsilon. \end{aligned} \quad \text{Equation 51}$$

In Equations 50 and 51, G_k and G_b are the kinetic energy production terms due to the mean velocity gradients and buoyancy respectively. The contribution from the fluctuating dilatation in compressible turbulence to the overall dissipation rate is Y_M . The turbulent Prandtl numbers for k and ε are represented by the constants σ_k and σ_ε , respectively. $C_{1\varepsilon}$, $C_{2\varepsilon}$, and $C_{3\varepsilon}$ are constants and S_k and S_ε are source terms defined by the user. The turbulent viscosity is subsequently modeled using Equation 52:

$$v_T = C_\mu \frac{k^2}{\varepsilon}, \quad \text{Equation 52}$$

where C_μ is a constant.

The standard k - ε model is known to perform well in free shear layers away from boundaries and wake regions (Menter, 1994), but breaks down in boundary layers with strong pressure gradients (Pope, 2010). These issues originate in the turbulent viscosity hypothesis and the equation for ε . Modifications to the constants can yield better results but these solutions are generally considered to be very *ad hoc* (Pope, 2010).

3.1.3 k - ε REALIZABLE MODEL

The k - ε Realizable model differs from the standard k - ε model in two ways. First, the turbulent viscosity formulation is modified to include a varying C_μ . Second, the equation for ε is replaced by a formulation from the exact equation for the transport of the mean-square vorticity fluctuation (Shih, et al., 1995). The k transport equation is the same as Equation 50. The transport equation for ε in the k - ε Realizable model is:

$$\begin{aligned} \frac{\partial}{\partial t}(\rho\varepsilon) + \frac{\partial}{\partial x_i}(\rho\varepsilon u_i) \\ = \frac{\partial}{\partial x_j} \rho \left[\left(\nu + \frac{v_T}{\sigma_\varepsilon} \right) \frac{\partial \varepsilon}{\partial x_j} \right] + \rho C_1 S \varepsilon - \rho C_2 \frac{\varepsilon^2}{k + \sqrt{\nu \varepsilon}} + C_{1\varepsilon} \frac{\varepsilon}{k} C_{3\varepsilon} G_b \\ + S_\varepsilon, \end{aligned} \quad \text{Equation 53}$$

where,

$$\begin{aligned} C_1 &= \max \left[0.43, \frac{\eta}{\eta + 5} \right], \\ \eta &= \frac{k}{\varepsilon} \sqrt{2S_{ij}S_{ij}}. \end{aligned}$$

The turbulent viscosity equation is the same as Equation 52, except C_μ is computed dynamically. This is accomplished by making it a function of the local flow field, k , and ε .

The k - ε Realizable model improves upon the results of the standard k - ε model for many flow cases, but still struggles with domains that contain both rotating and stationary fluid zones, i.e., rotating sliding meshes and multiple reference frames (Shih, et al., 1995).

3.1.4 k - ε RNG MODEL

The k - ε RNG model was developed with the statistical technique known as renormalization group theory (RNG). It is based on the fundamental assumption of the universality of small scales in turbulence, as first suggested by Kolmogorov (Orszag, et al., 1996). The transport equations for k and ε in the k - ε RNG model are:

$$\frac{\partial}{\partial t}(\rho k) + \frac{\partial}{\partial x_i}(\rho k u_i) = \frac{\partial}{\partial x_j} \left[a_k \mu_{eff} \frac{\partial k}{\partial x_j} \right] + G_k + G_b - \rho \varepsilon - Y_M + S_k, \quad \text{Equation 54}$$

$$\begin{aligned} \frac{\partial}{\partial t}(\rho \varepsilon) + \frac{\partial}{\partial x_i}(\rho \varepsilon u_i) \\ = \frac{\partial}{\partial x_j} \left[a_\varepsilon \mu_{eff} \frac{\partial \varepsilon}{\partial x_j} \right] + C_{1\varepsilon} \frac{\varepsilon}{k} (G_k + C_{3\varepsilon} G_b) - C_{2\varepsilon} \rho \frac{\varepsilon^2}{k} - R_\varepsilon + S_\varepsilon. \end{aligned} \quad \text{Equation 55}$$

It should be noted that there is a differential formulation of effective viscosity which account for effects of low Reynolds numbers in near wall regions. For high Reynolds number flow turbulent viscosity is calculated in the same manner as the standard k - ε models. The k - ε RNG models' most significant difference from the standard

model is the additional term in the ε equation improving the response to rapidly strained flows. R_ε is represented by

$$R_\varepsilon = \frac{C_\mu \rho \eta^3 (1 - \eta/\eta_0) \varepsilon^2}{1 + \beta \eta^3} \frac{\varepsilon^2}{k}, \quad \text{Equation 56}$$

$$\eta \equiv \frac{Sk}{\varepsilon},$$

$$\eta_0 = 4.38,$$

$$\beta = 0.012.$$

R_ε is not derived using RNG theory and is considered to be somewhat *ad hoc* (Pope, 2010). The k - ε RNG model also includes the effects of swirling flow, and analytical formulations of the turbulent Prandtl numbers (ANSYS, 2010). These improvements make k - ε RNG more applicable and accurate for a wider range of flows, yet improper model tuning can hamper results for near wall effects (ANSYS, 2010).

3.1.5 STANDARD k - ω MODEL

The standard k - ω model as originally developed by Wilcox (1988) uses transport equations of k , the turbulence kinetic energy and ω , the turbulence frequency to solve for the turbulent viscosity (Menter, 2009). These transport equations are:

$$\frac{\partial}{\partial t}(\rho k) + \frac{\partial}{\partial x_i}(\rho k u_i) = \frac{\partial}{\partial x_j} \left[\Gamma_k \frac{\partial k}{\partial x_j} \right] + G_k - Y_k + S_k, \quad \text{Equation 57}$$

$$\frac{\partial}{\partial t}(\rho \omega) + \frac{\partial}{\partial x_i}(\rho \omega u_i) = \frac{\partial}{\partial x_j} \left[\Gamma_\omega \frac{\partial \omega}{\partial x_j} \right] + G_\omega - Y_\omega + S_\omega, \quad \text{Equation 58}$$

where G_k and G_ω represent the production terms from the mean velocity gradients and ω , respectively. Γ_k and Γ_ω are the effective diffusivity of k and ω , respectively. Y_k and Y_ω are the dissipation due to turbulence from k and ω . Similar to the k - ε closure models, S_k and S_ω are user-defined source terms. The turbulent viscosity is modeled by:

$$\mu_t = a^* \frac{\rho k}{\omega},$$

Equation 59

$$\Gamma_k = \mu + \frac{\mu_t}{\sigma_k},$$

$$\Gamma_\omega = \mu + \frac{\mu_t}{\sigma_\omega},$$

$$a^* = a_\infty^* \left(\frac{a_0^* + Re_t/R_k}{1 + Re_t/R_k} \right),$$

$$Re_t = \frac{\rho k}{\mu \omega},$$

$$R_k = 6,$$

$$a_0^* = \frac{\beta_i}{3},$$

$$\beta_i = 0.072,$$

and for high Reynolds number flow $a^* = a_\infty^* = 1$.

Unlike any other RANS model $k-\omega$ does not require the use of damping functions in the near wall region. As a result the standard $k-\omega$ model has proven to be much more accurate than other models in the boundary sublayer. In addition, its simplicity yields a much more robust numerical stability (Menter, 1994). Unfortunately the standard $k-\omega$ model has a very high sensitivity to the freestream values specified for ω outside the boundary and shear layers. It has recently undergone several modifications to compensate for low-Reynolds number effects, compressibility, and shear flow spreading that are represented in ANSYS FLUENT. However, it still contains some ambiguity shown by Menter with a twofold variation in the turbulent viscosity through an ω sensitivity study (Menter, 2009).

3.1.6 k - ω SST MODEL

The k - ω Shear-Stress Transport (SST) model, blends the strength of the standard k - ω and k - ε models and borrows the shear stress term from the Johnson-King model (Menter, 1994). By doing this, the k - ω SST model performs very well in the viscous sublayer and far wall regions. This is accomplished by the addition of blending functions that are zero away from the boundary resulting in a k - ε type model and one inside the boundary layer resulting in a k - ω model (Menter, 2009). The transport equations for the k - ω SST model are:

$$\frac{\partial}{\partial t}(\rho k) + \frac{\partial}{\partial x_i}(\rho k u_i) = \frac{\partial}{\partial x_j} \left[\Gamma_k \frac{\partial k}{\partial x_j} \right] + \tilde{G}_k - Y_k + S_k, \quad \text{Equation 60}$$

$$\frac{\partial}{\partial t}(\rho \omega) + \frac{\partial}{\partial x_i}(\rho \omega u_i) = \frac{\partial}{\partial x_j} \left[\Gamma_\omega \frac{\partial \omega}{\partial x_j} \right] + G_\omega - Y_\omega + D_\omega + S_\omega. \quad \text{Equation 61}$$

In the k equation, \tilde{G}_k is still the production term for the turbulence kinetic energy from the mean velocity gradients but it is calculated in a different manner than for the standard k - ω model. D_ω is the cross-diffusion term used as a final blending term of the diffusion between the k - ω and k - ε models.

As demonstrated by the success of the Johnson-King model, consideration of turbulent shear stress can greatly influence accuracy in aerodynamic applications. To this extent, the turbulent viscosity formulation was modified to include turbulent shear stress in wall bounded flows, accomplished again by a blending function (Menter, 1994). The turbulent viscosity is represented by:

$$\mu_t = \frac{\rho k}{\omega} \frac{1}{\max \left[\frac{1}{a^*}, \frac{SF_2}{a_1 \omega} \right]}, \quad \text{Equation 62}$$

$$\sigma_k = \frac{1}{F_1/\sigma_{k,1} + (1 - F_1)/\sigma_{k,2}},$$

$$\sigma_\omega = \frac{1}{F_1/\sigma_{\omega,1} + (1 - F_1)/\sigma_{\omega,2}},$$

$$F_1 = \tanh(\Phi_1^4),$$

$$\Phi_1 = \min \left[\max \left(\frac{\sqrt{k}}{0.09\omega y}, \frac{500\mu}{\rho y^2 \omega} \right), \frac{4\rho k}{\sigma_{\omega,2} D_\omega^+ y^2} \right],$$

$$D_\omega^+ = \max \left[2\rho \frac{1}{\sigma_{\omega,2}} \frac{1}{\omega} \frac{\partial k}{\partial x_j} \frac{\partial \omega}{\partial x_j}, 10^{-10} \right],$$

$$F_2 = \tanh(\Phi_2^2),$$

$$\Phi_2 = \max \left(2 \frac{\sqrt{k}}{0.09\omega y}, \frac{500\mu}{\rho y^2 \omega} \right),$$

where, S is the strain rate magnitude, F_1 and F_2 are the blending functions, y is the distance to the nearest surface, and D_ω^+ is the positive portion of D_ω .

In addition, to prevent build-up of turbulence in stagnation areas, a production limiter was introduced. With all these model considerations, the k - ω SST model has consistently outperformed all other RANS models tested for aerodynamic applications (Menter, 2009).

3.1.7 LES

Large Eddy Simulations (LES) is generally considered the engineering research standard turbulence model. It is not a RANS model, but rather a filtered solution of the continuity, Navier-Stokes, and heat equations (Porté-Agel, et al., 2011). Through this filtering technique, LES resolves the larger energy-containing motions while modeling the subgrid-scale motions. The momentum equation contains the SGS stress tensor, which is most simply obtained with a turbulent viscosity model (Pope, 2010). This

formulation places in the turbulence model hierarchy between direct numerical simulations (DNS), where all scales are resolved down to the Kolmogorov length scale, and RANS where all scales are modeled (Pope, 2010). This provides for a much higher accuracy than RANS models produce. However, LES simulations require a much finer grid resolution and this increases computation time at least linearly. Most LES simulations require a filter and grid resolution such that 80% of the energy is resolved (Pope, 2010). For simulations in this thesis work a dynamic Smagorinsky-Lilly SGS model was used. Relaxation factors had to be adjusted to provide stability.

3.2 MODEL DESCRIPTION

The geometry of the NREL 5MW reference turbine was created in SolidWorks to the specifications in Jonkman et al. (2009) for rated conditions. This geometry was then exported into ANSYS DesignModeler, where the domain geometry was created. The domain was sized $2D$ (252m) upstream of the turbine, $20D$ (2520m) downstream of the first turbine, and $2.5D$ (315m) spanwise on either side of the turbines, where D is the diameter of the rotor. The turbines were placed at a hub height of 90 meters and the total height of the domain was set to $3D$ (378m). The two in-line turbines were then spaced αD apart, with α varied from 5, 10, and 15 (630m, 1260m, 1890m), respectively.

Meshing was performed in ANSYS Meshing using an unstructured tetrahedral mesh. Cell sizes were set to one meter on the blade faces and hubs, 0.5 meter on the blade tips. Cells were kept to a maximum size of 15 meters in the horizontal directions and ten meters in the vertical direction. Inflation layers were implemented on all solid surfaces with a maximum growth rate of 1.2. The meshes of all variations of the

stationary NREL 5MW reference turbine contained approximately two million cells. An example of the mesh can be seen in Figure 14.

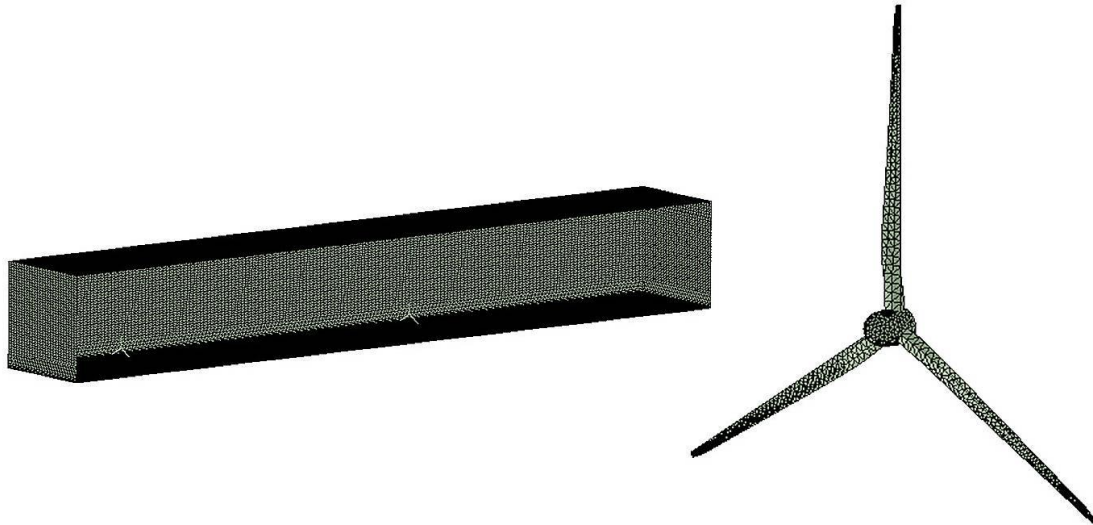


Figure 14 Cut-away of meshed domain for $\alpha = 10$ (left) and meshed turbine (right).

The disk model was created in a similar fashion to the turbine, with the non-porous disk having the same diameter (126m) as the swept area of the turbine. The disk had a thickness of one meter. Cell sizes were maintained at four meters on the disk faces and one meter on the disk edges. All other model measurements and constraints remained the same as the turbine case.

All CFD modeling was performed in ANSYS FLUENT V. 13.0. Models were run as transient simulations until they reached a semi-steady state. The inlet was set as a velocity inlet. The outlet was set as a pressure outlet. The sides and top were symmetry boundaries while the bottom and turbine or disk surfaces were set as wall boundaries. A user-defined function was employed to force a neutral atmospheric boundary layer (ABL) through the model with the hub height velocity set to the rated wind velocity (11.4m/s)

(Jonkman, et al., 2009). The user-defined function, set the neutral ABL using a power law to:

$$u = 11.4 \left(\frac{h}{90} \right)^{0.12} \quad \text{Equation 63}$$

A control model of an empty open channel flow domain was calibrated to ensure the neutral ABL maintained throughout the domain. The calibrated mode values were then used for the parametric study.

3.3 RESULTS

The results of all the simulations show a fairly strong correlation between all the turbulence models except the LES model. This deviation is likely a result of the grid requirements of the LES model. Because for each geometry a single mesh was run with each turbulence model, the LES model ran on a grid much coarser than required by the grid restrictions. This was cause for the LES model not resolving close to the 80% target energy scales and instead using the SGS model to produce the effects of the energy-containing scales. Since the SGS model is not as sophisticated as the RANS turbulence models, a significant difference between the results was expected and experienced. This result can be clearly observed in the streamwise velocity profiles shown in Figure 15.

The consistency of the RANS models throughout demonstrates the lack of separation occurring in this basic flow model, and does not show a distinct difference in turbulence models. However, as the turbine rotation produces more flow separation the resolution of the turbulence models will become more important. It is in this flow separation that the $k-\omega$ SST model has been seen to show a strong superiority over other two-equation turbulence closure schemes (Menter, 2009).

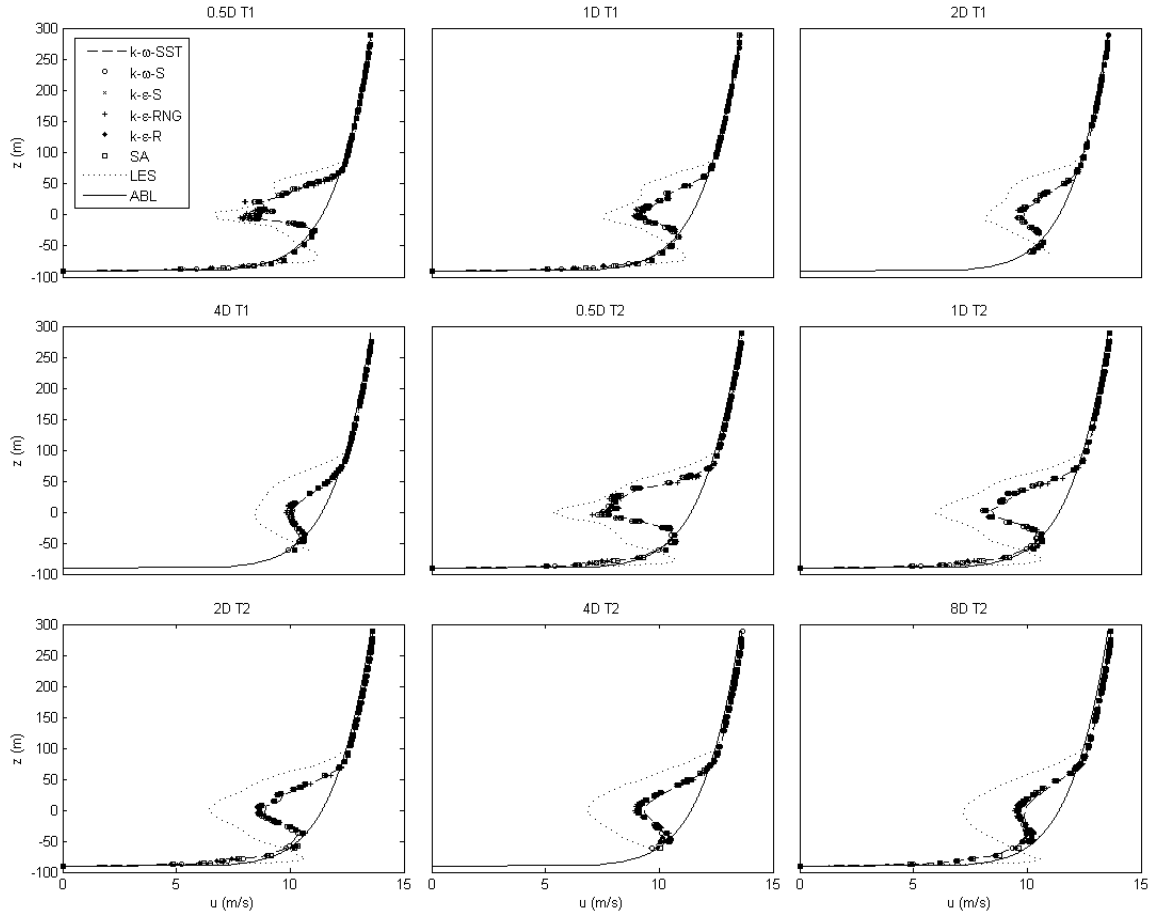


Figure 15 Velocity profiles (m/s) for selected turbulence models over two in-line stationary turbines spaced $5D$.

Figure 16 shows the streamwise velocity contours through a vertical plane following the centerline of the turbines for the $k-\omega$ SST turbulence model. For these cases, only a small velocity deficit was created downstream from each turbine. This wake was still present for the case of α equal to five, and nearly or completely resolved for the cases of α equal to 10 and 15. This is more clearly observed in Figure 17, showing the streamwise velocity profiles $1D$ upstream from the second turbine for each of the spacings.

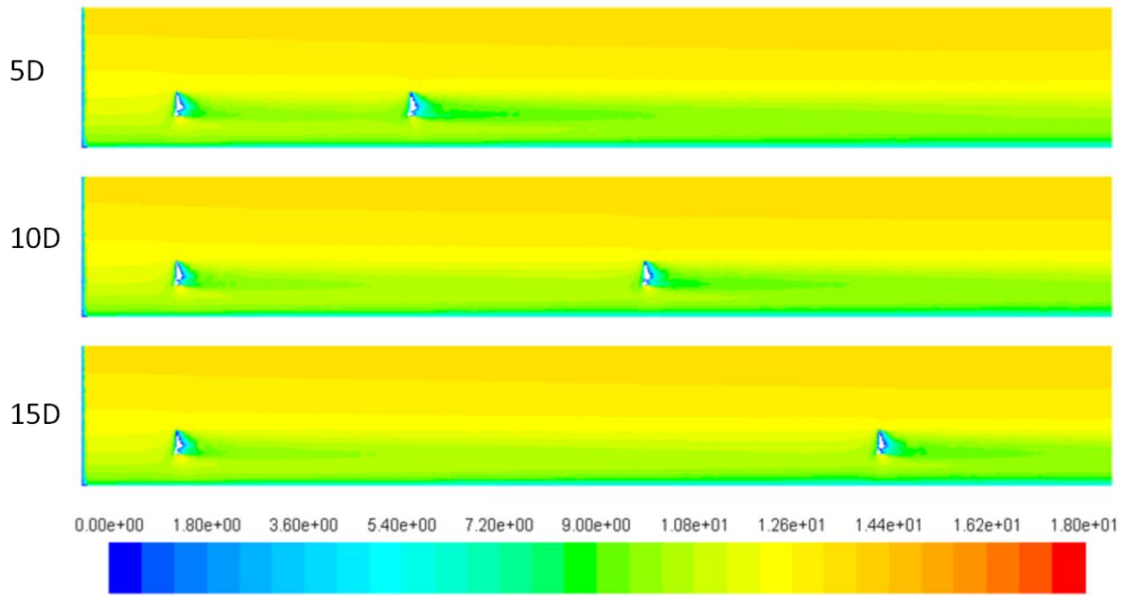


Figure 16 Streamwise velocity contours (m/s) on vertical bisecting plane for turbine spacings αD ($\alpha\{5, 10, 15\}$) $k-\omega$ SST.

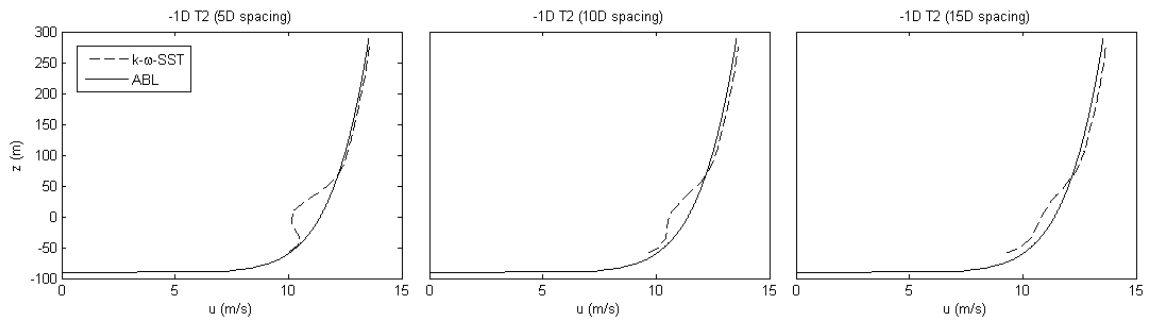


Figure 17 Streamwise velocity profiles $1D$ upstream of the second stationary turbine for spacings αD ($\alpha\{5, 10, 15\}$) $k-\omega$ SST.

It was observed that in Figure 16 a very small magnification of the velocity deficit occurred behind the second turbine for the case of α equal to five. This magnification can be seen to occur for all cases of α in Figure 18 showing the downstream velocity profiles $1D$ behind each turbine for all cases of α .

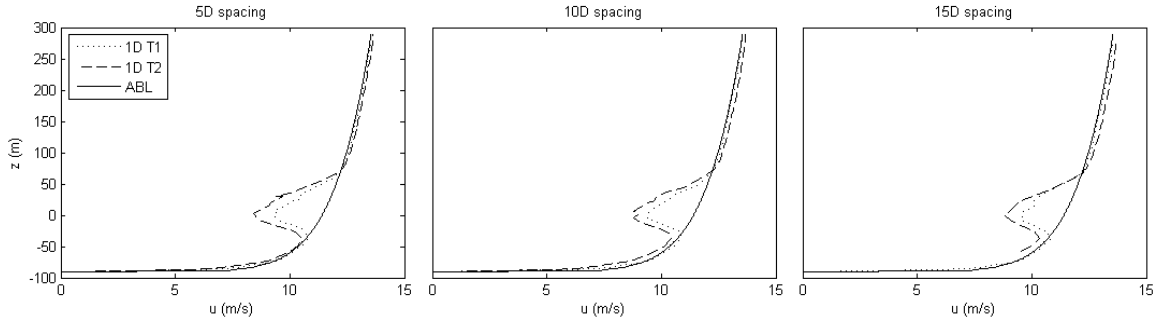


Figure 18 Streamwise velocity profiles 1D downstream of each stationary turbine for spacings αD ($\alpha\{5, 10, 15\}$) $k-\omega$ SST.

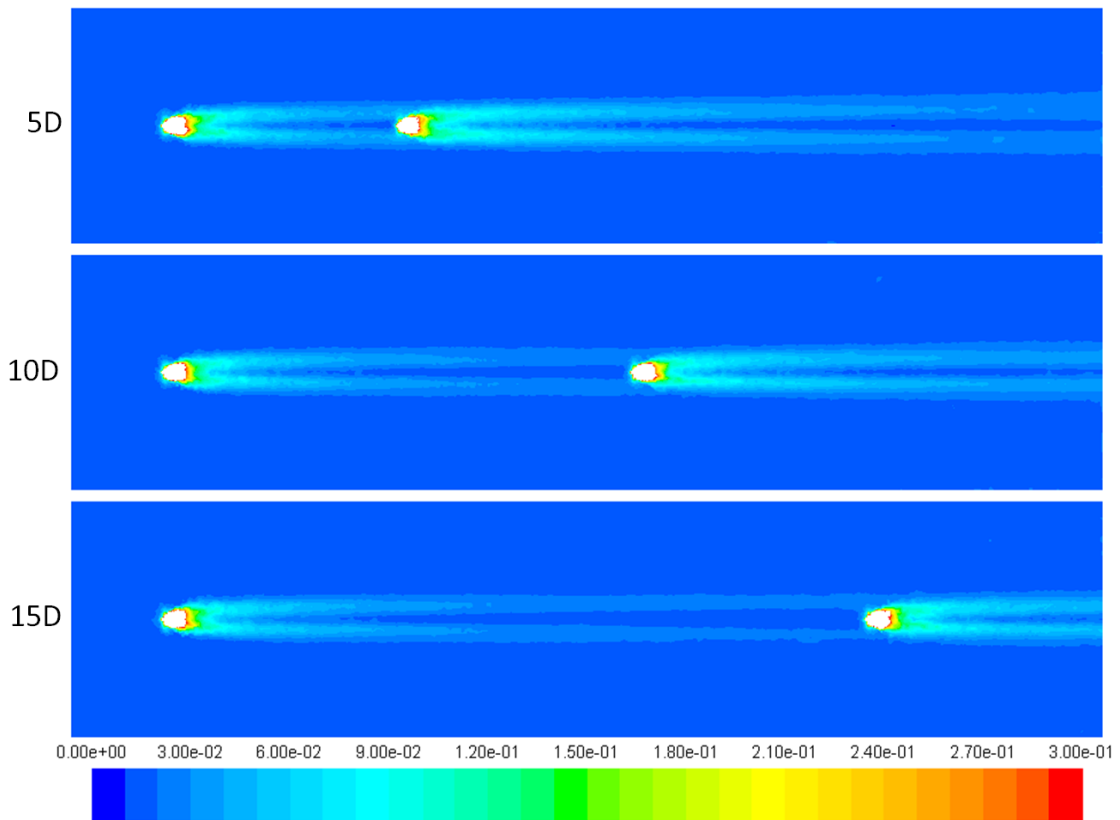


Figure 19 Vorticity magnitude (1/s) contours on horizontal plane, bisecting turbine hubs for spacings αD ($\alpha\{5, 10, 15\}$) $k-\omega$ SST.

Although in Figure 17 it would appear that the wake is nearly resolved before reaching the second turbine for α equal to 10 and 15, Figure 19 clearly displays an influence from the upstream wake for each case of α . Additionally, the wake maintains a stronger presence downstream of the second turbine when comparing the vorticity

downstream of the second turbine in the case of α equal to five to the vorticity downstream of the first turbine in the case of α equal to 15.

Figure 20 clearly shows that the second stationary turbine, for each spacing, experiences at least some influence from the upstream turbine, regardless of the resolution of the velocity profiles shown in Figure 17. Although the wake maintains a stronger presence downstream of the second turbine, Figure 20 shows that the vorticity is about equal $1D$ downstream of each of the turbines.

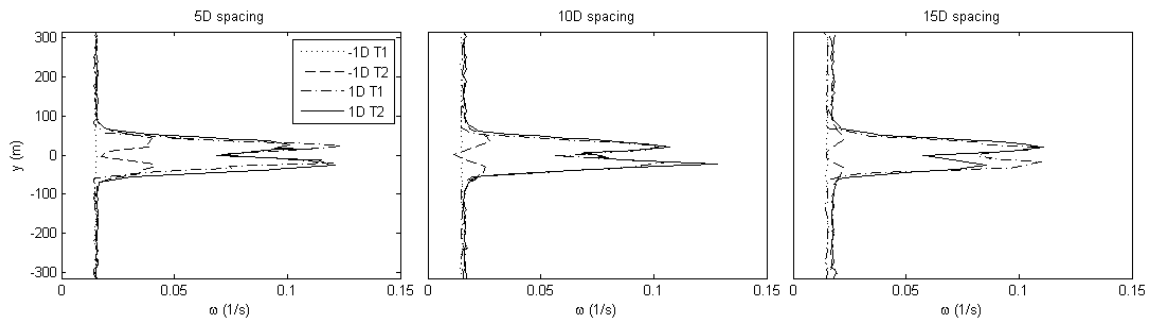


Figure 20 Vorticity magnitude on horizontal plane, bisecting turbine hubs, showing vorticity $1D$ up- and downstream of each turbine. Spacings αD ($\alpha\{5, 10, 15\}$) $k-\omega$ SST.

In contrast, the disk models were not able to reach the same semi-steady flow state because of significant separation and limited domain size. This result is shown in Figure 21 by the large variance in streamwise velocity profiles and further demonstrated in Figure 22 by the large variable coherent structures observed throughout the domain in the streamwise velocity contours. Although Figure 21 might indicate that there is some resolution well downstream of the second disk, Figure 22 shows that the resolution is still fairly random and does not resemble a well-formed ABL, as was demonstrated in Figure 15 and Figure 16.

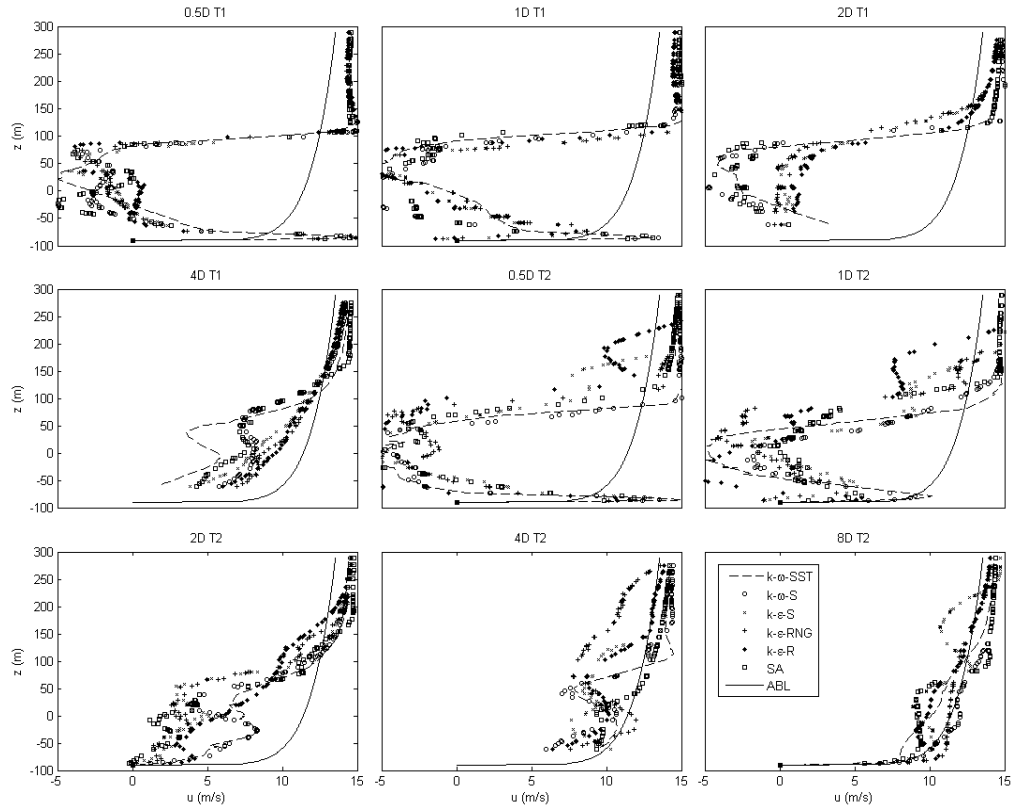


Figure 21 Velocity profiles (m/s) for selected turbulence models over two in-line non-porous disks spaced $5D$.

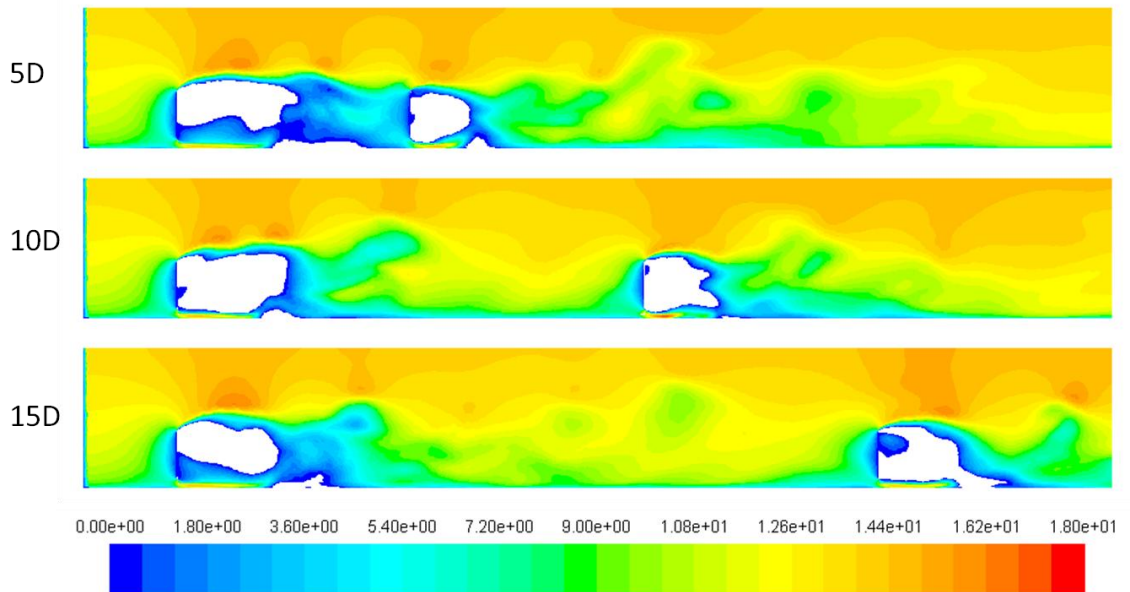


Figure 22 Streamwise velocity contours (m/s) on vertical bisecting plane for disk spacings αD ($\alpha \{5, 10, 15\}$) for $k-\omega$ SST.

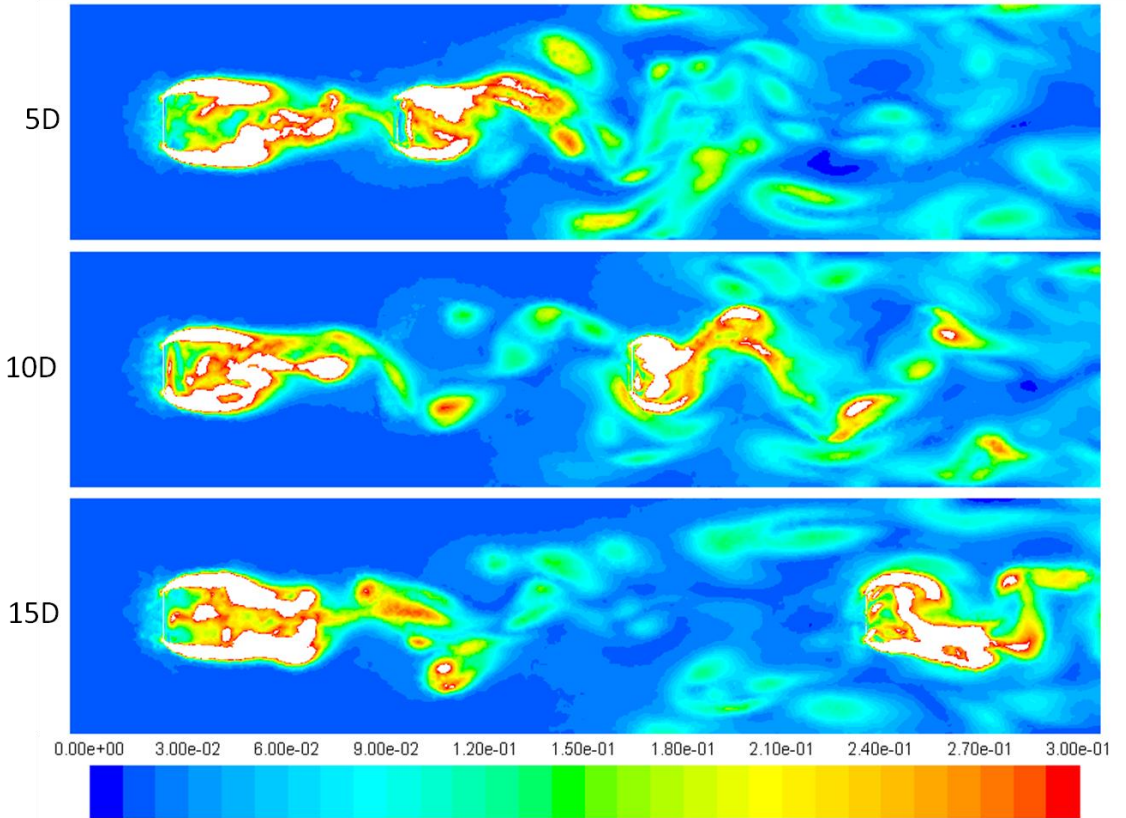


Figure 23 Vorticity magnitude (1/s) contours on horizontal plane, bisecting turbine hubs for spacings αD ($\alpha\{5, 10, 15\}$) $k-\omega$ SST.

Figure 23 shows the vorticity magnitude contours of flow over the in-line non-porous disks. From this it is once again apparent that the disk models did not reach a semi-steady flow state. Interestingly, Figure 23 displays structures indicating vortex shedding.

3.4 SUMMARIZING REMARKS

Many aspects of wake interaction were observed in this stationary study of turbine wake interaction. Although the velocity appeared to resolve prior to incident with the downstream turbines, for the cases of α equal to 10 and 15, magnification of the velocity deficit downstream of the second turbine did occur. The vorticity confirmed this

influence just prior to the second turbines for all cases of α and maintained a stronger presence far downstream of the second turbine.

Due to the lack of separation in these stationary cases, very little discrepancy could be found between the RANS turbulence models. However, the separation effects with rotation will become very important. In previous studies, the $k-\omega$ SST turbulence model was shown to have superior performance in aerodynamic applications (Menter, 2009; Tachos, et al., 2010). For this reason, the $k-\omega$ SST turbulence closure scheme would be the best to model separation and wake structure. The proceeding studies of rotating turbines will solely utilize the $k-\omega$ SST turbulence model.

In the following chapter, the development, structure, interaction, and resolution of turbine wakes will be studied with the additional complexity of rotating turbines. These studies will investigate in-line turbines, as well as a single turbine. A grid independence study is also performed to extract an accurate pressure distribution for use in a separate collaborative structural study of non-linear effects of flexible turbine blades.

CHAPTER 4. ROTATING TURBINE STUDY

Three rotating studies were performed. The first was a study of wake interaction performed on two rotating, in-line NREL 5MW reference turbines (Jonkman, et al., 2009) spaced $5D$. The objective of these studies was to examine the flow characteristics experienced by the downstream turbine and, in the far wake region, with a mind toward spacing and fatigue loading. The second study was performed on a single rotating NREL 5MW reference turbine (Jonkman, et al., 2009) with $20D$ spacing downstream. The objective of this study was to examine the wake resolution. The third study was a grid independence study on a single rotating NREL 5MW reference turbine (Jonkman, et al., 2009). This study examined pressure distributions on the turbine blades. The $k-\omega$ SST turbulence model was used for all models in these studies. All models were run on a four parallel processor system to demonstrate the capabilities of RANS models on non-supercomputer systems.

4.1 WAKE INTERACTION MODEL DESCRIPTION

The geometries for the rotating turbine models were created in the same manner as the stationary turbine model with the exception of added rotating domains. These cylindrical domains were 150 meters in diameter and 20 meters wide, encompassing each turbine. The rotating domains allow for a sliding mesh computation.

The meshes were also created in the same manner as the stationary turbine model with the exception of added restrictions on the rotating domain surfaces. The front and

back faces of the rotating domains were constrained to seven meter cell sizes and the cylindrical surfaces of the rotating domains were restricted to four meter cell sizes. With these modifications all three models contained approximately 2.15 million cells. The rotating turbine mesh is shown in Figure 24.

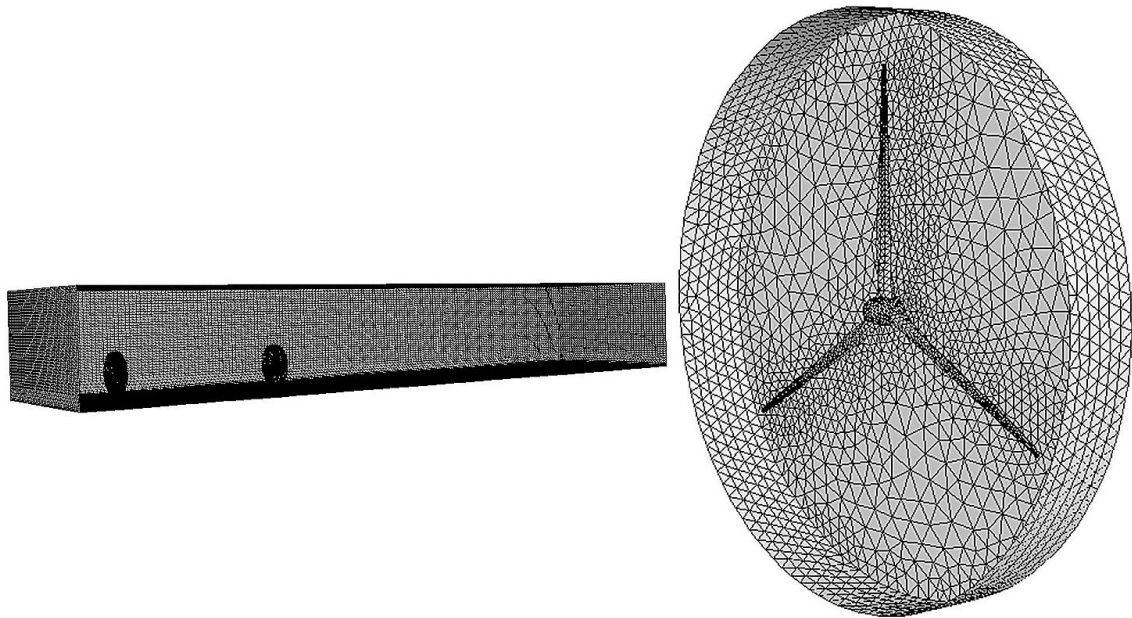


Figure 24 Cut-away of meshed domain for $\alpha = 5$ (left) and meshed turbine enclosed in rotating domain (right).

The ANSYS FLUENT setup of the rotating models was a bit more involved than for the stationary models. For complex geometries with unsteady interactions, a sliding mesh must be used (ANSYS, 2010). The rotating domains and turbines were set to rotate at the rated angular velocity of 12.1 revolutions per minute (Jonkman, et al., 2009). The remaining pre-processing was performed in the same manner as for the stationary $k-\omega$ SST model. All models were run as transient calculations until they had reached a semi-steady state; this took ten minutes in real time.

4.2 WAKE INTERACTION RESULTS

As expected, the parametric study of a stationary turbine and non-porous disk bounded the flow characteristics of the rotating turbine. Figure 25 illustrates that the rotating turbine aligns much closer to the results of the stationary turbine in the near turbine wake region. The added rotational velocity of the wake, however, carried the wake effects further downstream resulting in the downstream turbine experiencing a much larger velocity deficit and lower power output. It can be seen that by $8D$ downstream of the second turbine the wake has been nearly resolved.

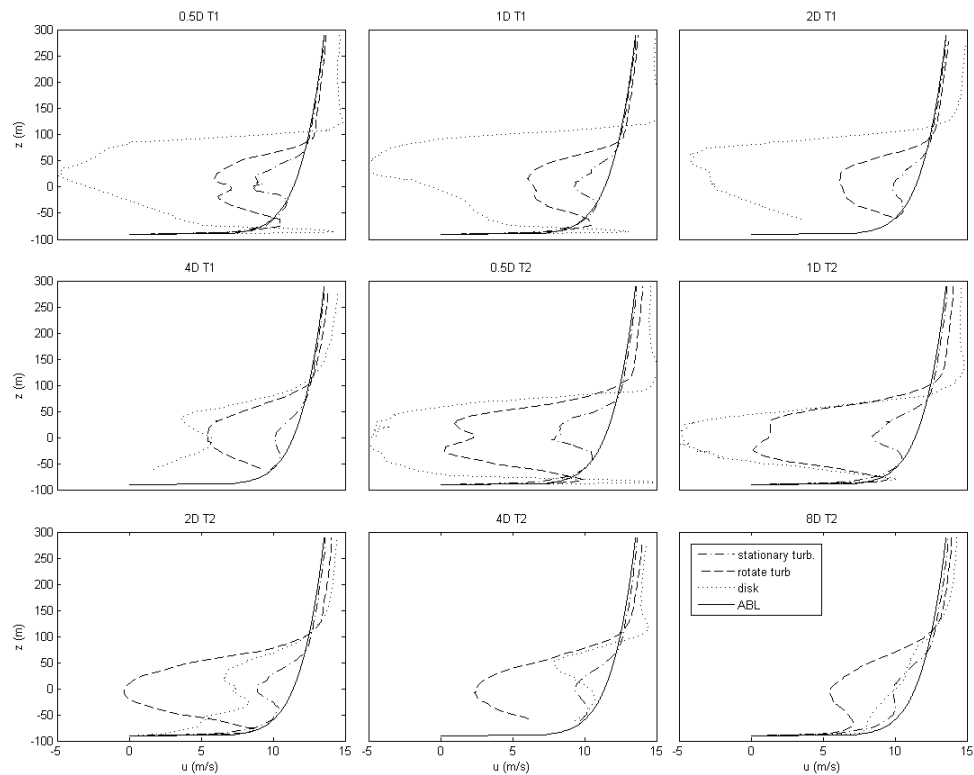


Figure 25 Velocity profiles (m/s) for $k-\omega$ SST and spacing of $5D$, comparing the stationary turbine, rotating turbine, and non-porous Disk.

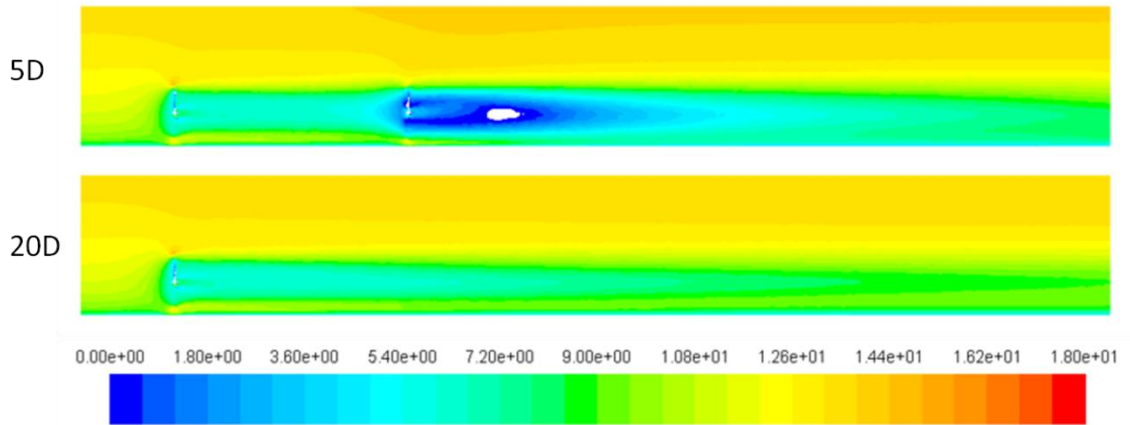


Figure 26 Streamwise velocity contours (m/s) on vertical bisecting plane comparing two turbines spaced $5D$ and single turbine with $20D$ spacing downstream, $k-\omega$ SST was used.

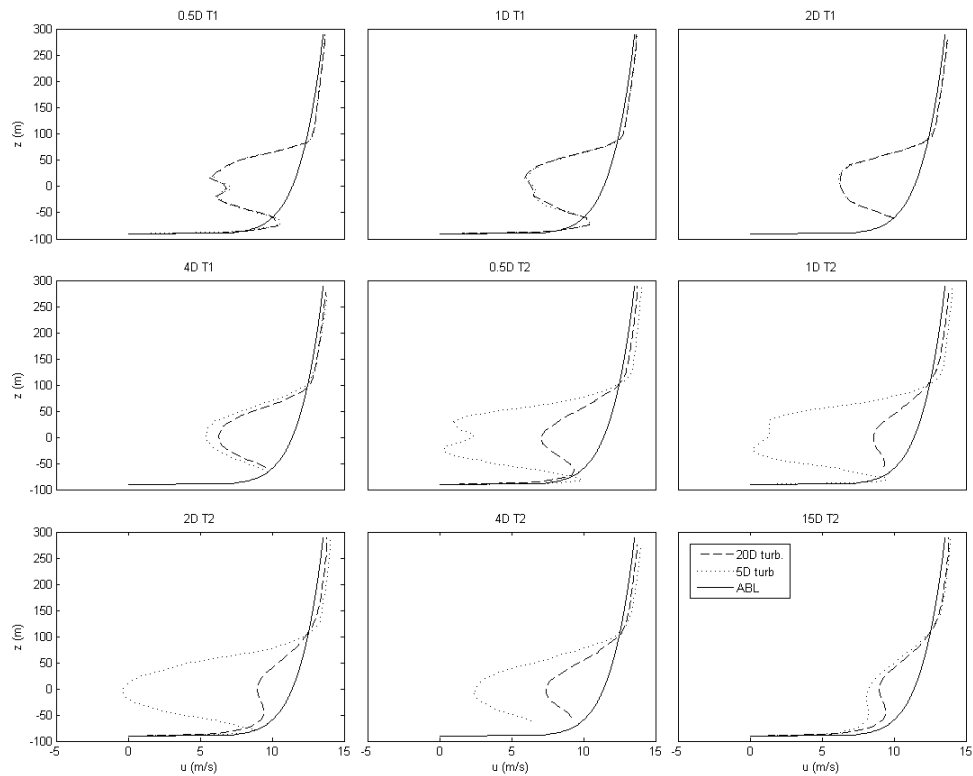


Figure 27 Velocity profiles (m/s) comparing single turbine with $20D$ spacing downstream to two turbines spaced $5D$ with $15D$ spacing behind second turbine, $k-\omega$ SST was used.

Figure 26 confirms this resolution. Figure 25 and Figure 26 demonstrate that the velocity deficit is magnified significantly behind the second turbine, with a small area of recirculation approximately $2D$ downstream of the second turbine. When the two turbine

model is compared to the one turbine model in Figure 27, the wakes align very closely just behind the first turbine, as should be expected. However, just in front of the second turbine there is a slight increase in velocity deficit. The velocity deficit at 4D behind the first turbine translates to a power loss of approximately 67 percent.

Vorticity is very insightful when studying wake interactions. Figure 28 shows a distinct magnification of vorticity downstream of the second turbine. The structure of the wake expands as it disperses downstream of the turbines. The two well-defined strips of increased turbulence indicate the signature helical structure of the turbine wake caused by the tip vortices. As noted by Porté-Agel et al. (2011) this wake structure cannot be replicated with an ADM, rotating or stationary. However, as a result of the modeling of the actual turbine blades, even without an LES model, the tip vortices are well-defined.

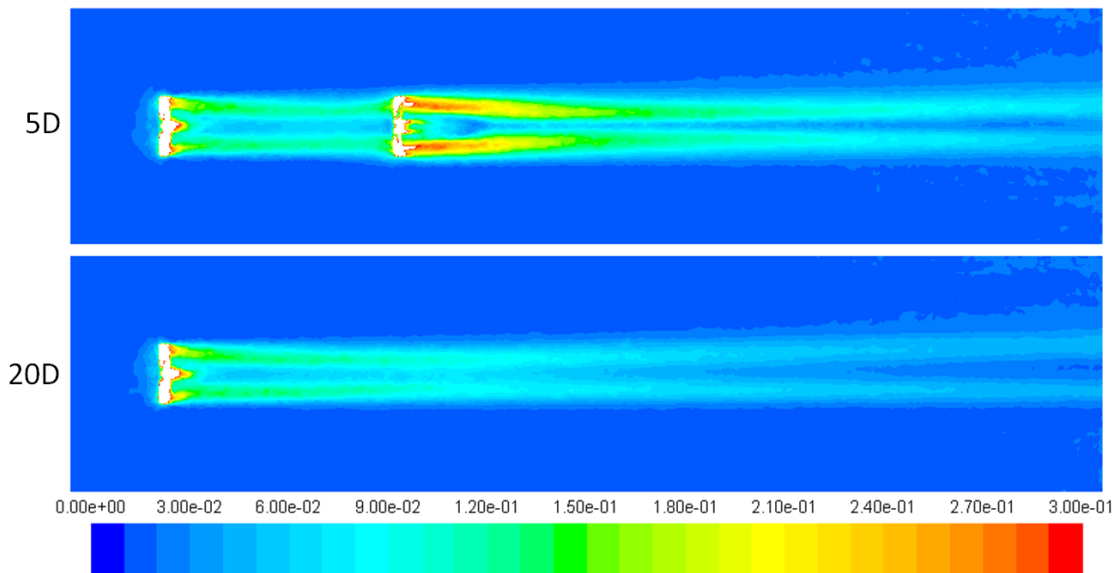


Figure 28 Vorticity magnitude (1/s) on horizontal plane bisecting turbine hubs, for in-line turbines 5D spacing (top), single turbine 20D spacing downwind (bottom).

Figure 29 illustrates further definition of the wake structure in the iso-surfaces. It is clear from the iso-surfaces that the wake contains a clearly defined helical structure surrounding a more stationary center core. This is not entirely accurate. With a finer grid

resolution, it may have been possible to resolve the inner helical structure as seen in the simulations of Fletcher & Brown (2010).

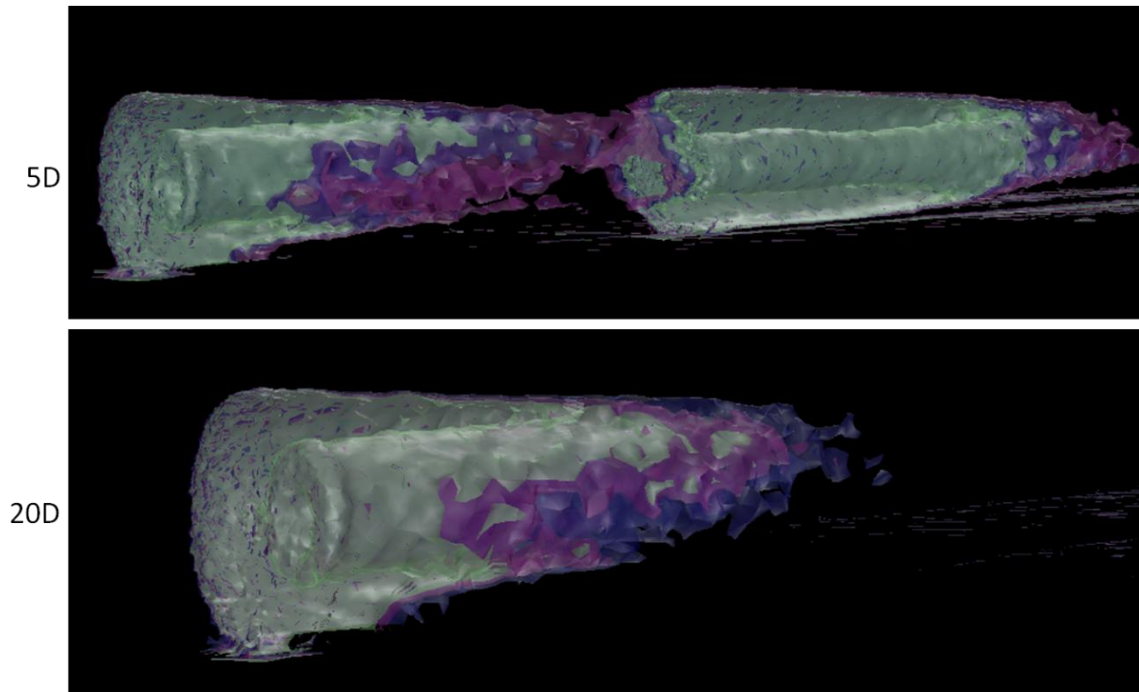


Figure 29 Vorticity magnitude iso-surfaces (blue = 0.12 1/s, magenta = 0.13 1/s, green = 0.14 1/s), for in-line turbines 5D spacing (top), single turbine 20D spacing downwind (bottom).

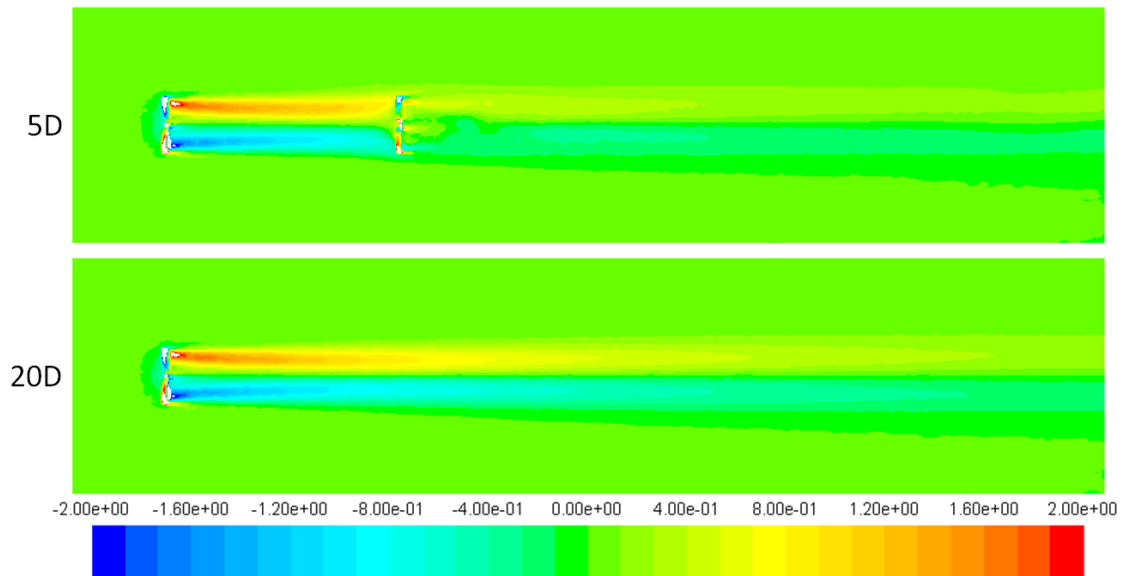


Figure 30 Vertical velocity (m/s) contours on horizontal plane bisecting turbine hubs, for in-line turbines 5D spacing (top), single turbine 20D spacing downwind (bottom).

The vertical velocity contours seen in Figure 30 show a clear direction and magnitude of wake rotation. Interestingly the disturbance caused by the second turbine actually acts to slow the rotation, even though the turbines are rotating at the same angular velocity and direction. The disturbance is great enough that the two in-line turbines create a slower rotating wake at 15D behind the last turbine than at 15D behind just the single turbine.

As an interesting note of comparison, the data from the velocity profiles published by Porté-Agel et al. (2011) was extracted and compared to the current case of a single rotating turbine. Since two different turbines were studied, one scale-model in a wind tunnel LES simulation and the current full scale RANS model, all length units were non-dimensionalized with respect to the turbine diameter and all velocity units were non-dimensionalized with respect to the ABL velocity at hub height. The compared velocity profiles are shown in Figure 31. The velocity profiles correlate very closely. It should be noted, however, that no Reynolds number scaling has been applied.

Pressures were published in literature for studies on the NREL 5MW reference turbine (Bazilevs, et al., 2010). For this thesis work it will be used as a means of partial validation. In the study performed by Bazilevs et al. (2010), it was seen that the NREL 5MW turbine experienced a maximum pressure of 1.2 kPa on the leading tip of the blade. This value was approximately matched at 1.41kPa in the current study. It should be noted that in the study by Bazilevs et al. (2010) the angular velocity of the blade and incident wind field were slightly less than the rated conditions used for this study. The study by Bazilevs et al. (2010) did not include a grid independence study and deficiencies

in their results were reported as a result of coarse grid resolution. In the section that follows a grid resolution will prove its worth.

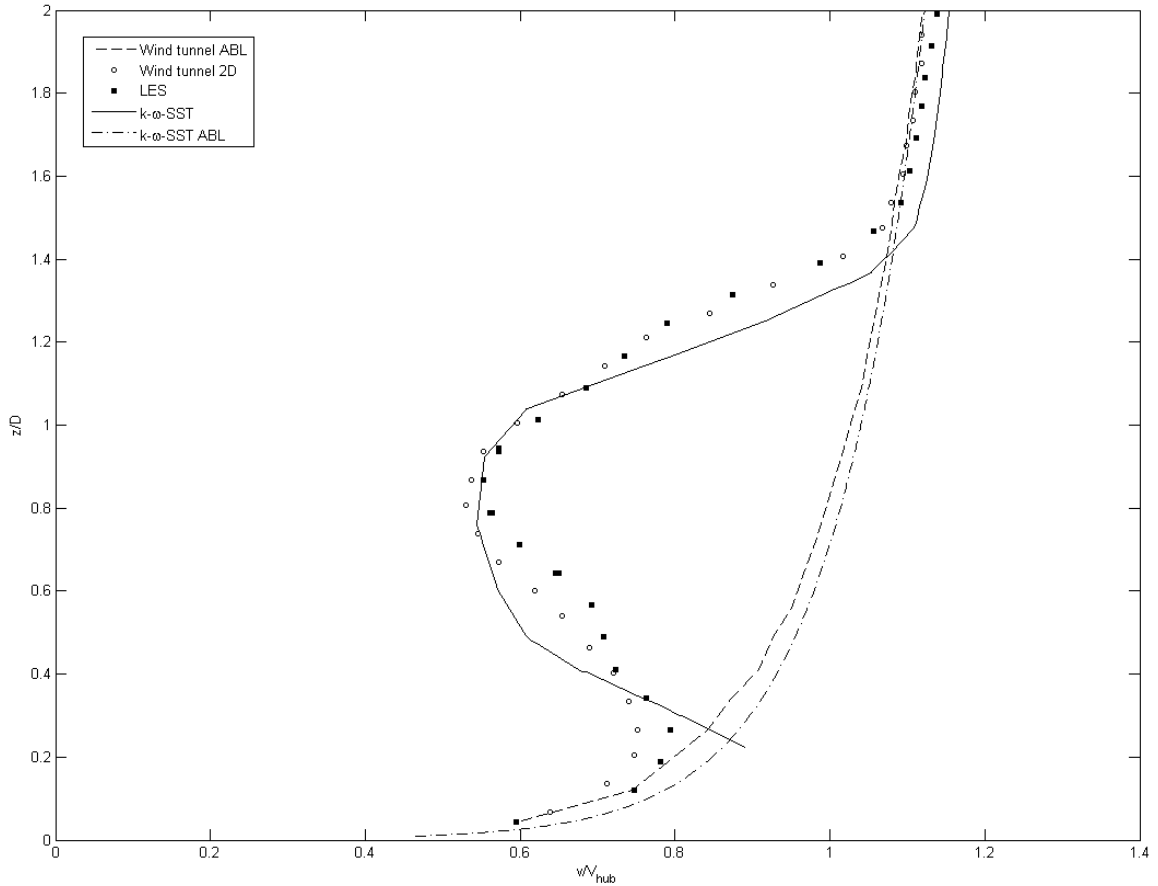


Figure 31 Non-dimensionalized streamwise velocity profiles 2D downstream of turbine, comparison between current study and data extracted from highly resolved LES simulations (Porté-Agel, et al., 2011).

4.3 GRID INDEPENDENCE MODEL DESCRIPTION

The grid independence model was set up in a very similar manner to the wake interaction models, with the exception of the domain and mesh sizes. For the grid independence models, the domain included only one rotating turbine located 2D from the inlet and extended only 5D downstream of the turbine. The mesh sizes were then varied on the turbine and rotating domain surfaces. Table 2 shows the various mesh restrictions and model cell counts.

Table 2 Grid independence mesh restrictions

Mesh size (x10 ⁶)	Blade Face Cell Size (m)	Blade Tip Cell Size (m)	Rotating Domain Face Cell Size (m)	Rotating Domain Cylinder Cell Size (m)
0.789	1	0.5	7	4
0.951	0.8	0.2	5	4
1.09	0.65	0.15	4	4
1.27	0.5	0.1	4	4
5.43	0.1	0.05	2	2

4.4 GRID INDEPENDENCE RESULTS

The grid independence study had some interesting findings the most interesting of which is the validating point. The asymptote of maximum pressure that is reached as the cell size diminishes is very nearly the same as the Bernoulli calculated tip pressure. The Bernoulli equations states:

$$p + \frac{1}{2}\rho V^2 + \rho gh = constant \quad \text{Equation 64}$$

If Equation 64 is solved by superposition, using the rotating tangential velocity of the blade at the tip, and then using the incident wind speed, the theoretical maximum pressure magnitude can be achieved. For the current case that maximum theoretical pressure was found to be 3.9 kPa and the maximum pressure found in the study was 3.8kPa.

As seen in Figure 32, the pressure exerted on the blades increases dramatically and levels of approximately 3.5 kPa at the case of 1.09 million cells with grid refinements of 0.65 meters on the blade surfaces. This is a very small change from the previous case but with dramatic results. These results illuminate the importance of performing a grid independence study and refining wall boundary layers. This is even more evident when reflecting on the two-way coupling LES study performed by Bazilevs et al. (2010, 2011).

In this study, they reported maximum blade pressures of 1.2 kPa, but also noted that some flow characteristics were deficient as a result of grid refinement. In the present thesis work, a similar maximum pressure was found in section 3.3, however, with grid refinement, the maximum pressure was shown to approach the theoretical maximum.

Although this maximum pressure can be calculated by hand with the Bernoulli equation, the distribution of the pressure along the blade does require CFD simulation. This distributed pressure is the most important result from the simulation because it causes significant torque and non-linear bending in the very anisotropic blade materials. The distributed pressures are presented in the pressure contours of Figure 33. These distributions would suggest that investigation into non-linear beam effects should be pursued.

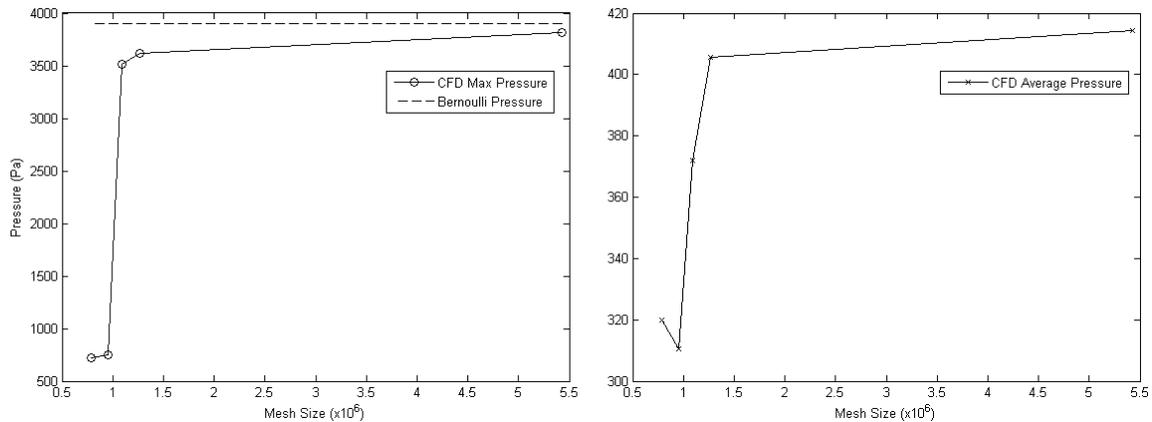


Figure 32 Pressure (Pa) vs. mesh size. Maximum pressure is asymptotic to Bernoulli pressure as mesh size increases (left). Average pressure is asymptotic as mesh size increases (right).

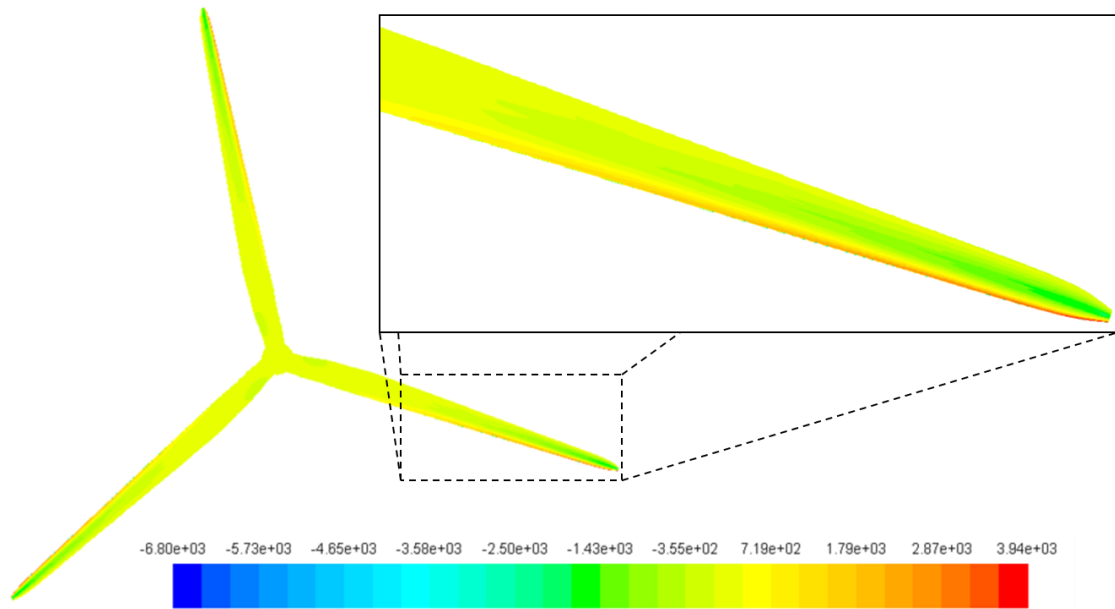


Figure 33 Pressure distribution on blades (Pa).

4.5 DISCUSSION ON STRUCTURAL APPLICATION

Increased demand for wind energy has pushed an evolution of the size of wind turbines. Motivated by the cube of velocity being proportional to power and higher wind speed aloft, wind turbine blades have increased in size considerably. This has greatly increased the flexibility of turbine blades, consistent with the assumption of Euler-Bernoulli beam theory, where stiffness is inversely proportional to beam length. As blades keep increasing in length they become more prone to non-linear effects. These effects can cause undesired vibration and resonance. In addition, turbulence can compound these effects (Moriarty, et al., 2002). Interaction between flow fields and rotating flexible blades has received very little attention; this has motivated Dr. Paul Heyliger to perform a joint fluid-structure interaction study. Here, the wind loads found in this thesis work are applied (in a one-way coupling) to a non-linear model to identify

and quantify the primary influences of the turbine blades' structural response. The following section attempts to give a brief overview of Dr. Heyliger's work.

Non-linear effects increase beam stiffness allowing them to carry greater loads for the same deflection. This becomes increasingly important to understand and analyze as beams become more flexible. As an example for a cantilever beam loaded uniformly, non-linear stiffening will allow it to carry almost three times the load analyzed using a linear Euler-Bernoulli beam theory. This is shown clearly in Figure 34.

For this study the computational model was based on an updated Lagrangian formulation of deformation. A Colorado State University coded finite element model was implemented using eight-noded 3-D brick elements. The simplest mesh that would capture the primary physics was used to determine the influence of kinematic variable and the strength of the geometrically non-linear response. The structural model of the turbine blade included skins and shear webs made of E-glass/epoxy laminate with a balsa core, and spar caps made of A260 fabric laminate (Griffin, 2002).

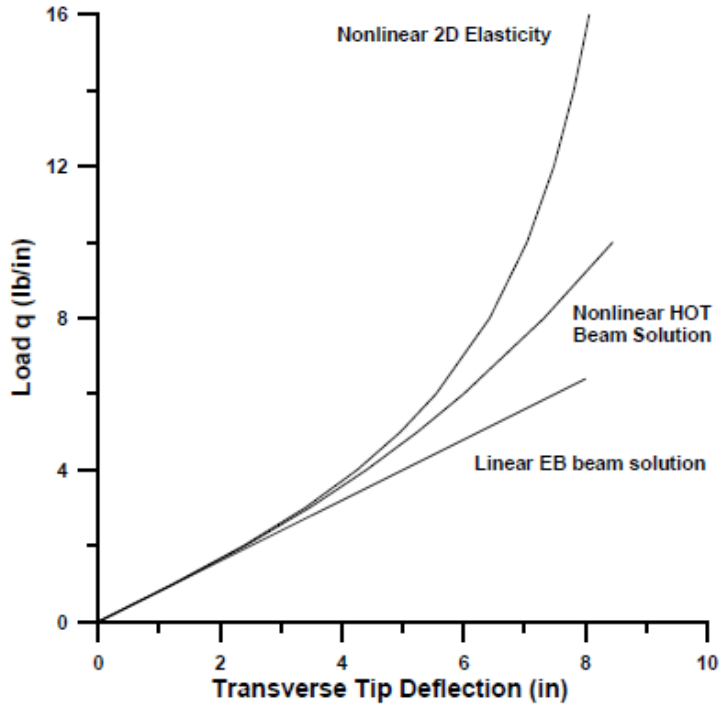


Figure 34 Load vs. tip deflection for linear Euler-Bernoulli, non-linear higher order, and non-linear 2D Lagrangian beam solutions (Heyliger, et al., 2011).

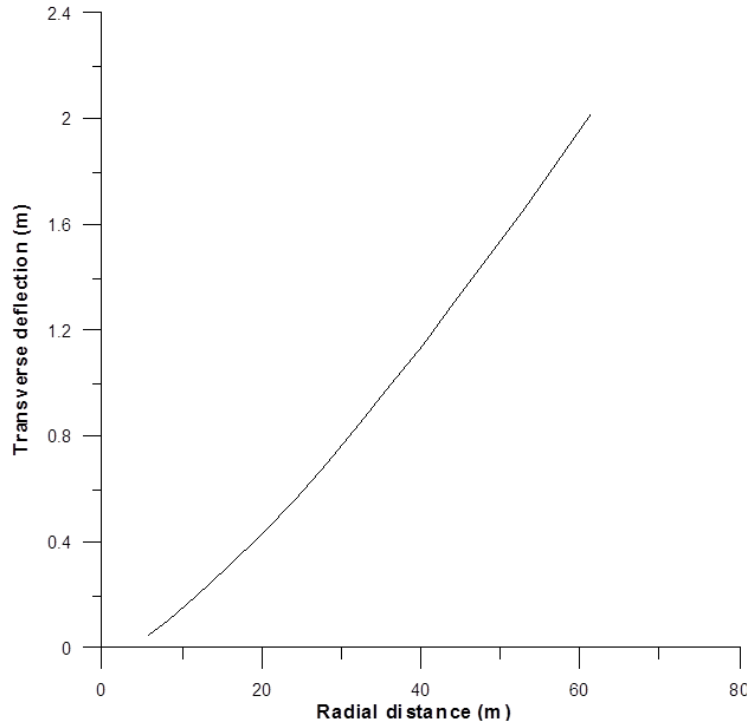


Figure 35 Radial distance vs. transverse deflection results of non-linear Lagrangian analysis.

The deflections seen in Figure 35 were found to be consistent with the allowable tip deflections for a 63 meter blade (TPI Composites, Inc., 2004). The non-linear stiffening was found to be between six and ten percent for the rated velocity. Transverse shear contributions made up approximately ten percent of the total strain energy. The deformation of the normal from transverse blade compression was found to be between 15% and 18% of the total deformation; this is both unusual and significant. Although the non-linear stiffening helps the structure and is conservative, the shear and transverse normal strain energies are likely not represented by the standard Euler-Bernoulli 1D beam models. This confirms the need for non-linear analysis to further understand and predict the structural responses of turbine blades to wind loads.

4.6 SUMMARIZING REMARKS

The additional complexity of blade rotation provided vast insight into the development, structure, interaction, and resolution of wind turbine wakes. Very little wake resolution was seen prior to incident with the downstream turbine, which translates into a reduced power output. Substantial velocity deficit magnification was also observed downstream of the second turbine. The structure of the wake was investigated using vorticity, and revealed a clear helical rotation. The iso-surfaces of vorticity illustrated an inner and outer wake structure, showing some affect from the turbine hub. Interestingly, it was found that the second turbine had some cancelling effect on the vorticity as the vorticity downstream of the second turbine resolved quicker than the vorticity behind the single turbine.

The grid independence study found that the maximum pressure on the turbine blades asymptotically approaches the theoretical Bernoulli maximum pressure. However

for a clear picture of blade loading, a full CFD pressure distribution on the blade surfaces is needed. The pressure distributions from this study were one-way coupled to a separate collaborative non-linear beam study. It was found that non-linear effects play a significant role in the blades structural response and cannot be ignored. This further highlights the need to compute an accurate pressure distribution, and insuring grid independence is essential for accuracy.

This study was a first step into modeling wind turbine wake interaction. It sought to illustrate the capabilities of desktop computing by performing all simulations on four parallel processors. This thesis work proposed that wake structure and interaction can be best captured using a resolved rotating turbine with RANS analysis as opposed to ADMs with LES analysis. It has shown a strong ability to accurately study wind turbine wake structures and interactions. It has also raised questions for further studies which will be addressed in the concluding chapter.

CHAPTER 5. CONCLUSIONS

As concerns continue to increase over resource availability, energy prices, environmental impacts, and worldwide population growth, renewable energy production becomes paramount in maintaining current and future energy demands. Wind energy has prevailed as the most cost-effective source of renewable energy production. As wind turbines reach higher into the atmosphere, rotor diameters increase and wind farms expand beyond 20 km in length. The need for advanced computational modeling is ever increasing.

5.1 SUMMARY

Wind turbine aerodynamic analysis has its roots in helicopter and propeller aerodynamics starting with Glauert (1935) and had advanced empirically until recently being mostly handed off to advanced CFD analysis. In the past decade many studies have built the foundation for understanding single and entire wind farm aerodynamics. Many CFD techniques have been utilized from RANS to LES modeling actuator disks to fully resolved rotating turbines.

The present study investigated several models to gain understanding into wake interaction of wind turbines and pressure distributions on turbine blades. This thesis work proposed that wake structure and interaction is best captured using a resolved rotating turbine with RANS analysis as opposed to ADMs with LES analysis. As a first step, a parametric study of turbulence models was performed for several RANS models and a LES model. It was found that the $k-\omega$ SST turbulence closure scheme was the most

appropriate to perform the computationally intensive and highly separable rotating turbine model.

Several rotating turbine models were run to study wake interaction and resolution. These models were run with desktop computing capabilities in mind. Neutral ATB layers were forced through the models. They were very successful in showing the formation, structure, interaction, and resolution of wind turbine wakes.

A grid independence study was performed with mind toward a future non-linear beam theory study of blade response. Maximum pressures were found to asymptotically approach the theoretical Bernoulli pressure maximum, validating the model and demonstrating the importance of grid resolution and independence studies.

The resulting blade pressures were then analyzed using a non-linear Lagrangian finite element code developed by Dr. Paul Heyliger. His results demonstrated the need for non-linear beam analysis on large flexible turbine blades.

5.2 KEY RESULTS

The key results for the stationary turbine model are as follows:

- It was found that although the velocity appeared to resolve prior to incident with the downstream turbines, in the cases of α equal to 10 and 15, magnification of the velocity deficit downstream of the second turbine did occur. The vorticity confirmed this influence just prior to the second turbines for all cases of α and maintained a stronger presence far downstream of the second turbine.
- It was discovered that for a stationary turbine with moderate grid refinement and little flow separation, all the RANS models displayed very strong agreement. The mesh was not refined enough to accurately perform the LES simulation because

the energy-containing length scales were over dependent on the SGS model. Since separation effects from rotation are critical, as found in previous studies from Menter (2009) and Tachos et al. (2010), the $k-\omega$ SST model was superior for aerodynamic applications. The $k-\omega$ SST model was the most appropriate for the study of rotating turbines.

The study of rotating turbines provided much insight into the formation, structure, interaction, and resolution of wind turbine wake interactions. This study confirmed the postulation that to truly model wake interactions, a resolved rotating turbine with a RANS analysis provides more insight than an ADM with LES analysis. The key results for the rotating turbine studies are as follows:

- It was seen that very little wake resolution had occurred prior to incident with the downstream turbine, translating into a reduced power output. Substantial velocity deficit magnification was also observed downstream of the second turbine, translating into significant near-wake downstream power losses. However, wakes were shown to nearly resolve by approximately 15 diameters downstream of the last turbine.
- Vorticity revealed a clear helical rotation. The iso-surfaces of vorticity illustrated an inner and outer wake structure, showing some affect from the turbine hub. The second turbine had some cancelling effect on the vorticity as the vorticity downstream of the second turbine resolved quicker than the vorticity behind the single turbine.

The grid independence study found that:

- The maximum pressure on the turbine blades asymptotically approaches the theoretical Bernoulli maximum pressure.
- For a clear picture of blade loading, a full CFD pressure distribution on the blade surfaces is needed.
- The pressure distributions from this study were one-way coupled to a separate collaborative non-linear beam study. Dr. Heyliger found that non-linear effects play a significant role in the blades structural response, which would likely not been found by a standard Euler-Bernoulli beam model, solidifying the need for non-linear structural models as well as improved coupled fluid-structure interaction. This further highlights the need to compute an accurate pressure distribution, and insuring grid independence is essential for accuracy.

5.3 SUGGESTIONS FOR FURTHER RESEARCH

This study provides a first step in research and insight into wind turbine wake interaction for the purpose of optimization of turbine spacing for maximum power output and minimum fatigue damage. It also raises areas for further research. Slightly removing the restriction of desktop computing capabilities would allow for vast model improvement and expansion. The next step of research would be to perform a grid independence study on the in-line rotating turbine model. A parametric study of spacing could be performed on this resolved model to obtain an optimum in-line spacing. This would provide a much clearer resolution of the wake structure and interaction. The greater question of wind farm wake interaction still postures to be answered. The resolved turbine model could be used to validate an ALM which could be applied to a full wind farm simulation.

The current thesis work was limited to the condition of a neutral ABL. In reality, the diurnal cycle consists of ever changing convective and stable ABL conditions. It would be very insightful to incorporate some of these conditions into the simulations. Ideally these conditions could be included in a full wind farm simulation.

As stated by Ian James (1994), “Comprehensive complexity is no virtue in modeling, but, rather, an admission of failure.” This is essential for all modeling. Simplifications must be made in a manner that does not adversely affect the desired physics too greatly. The modeling in this thesis is admittedly not comprehensive, but has made an effort to simplify the problem while maintaining the desired physics. It is to this effect that future work must also be performed.

REFERENCES

- ANSYS. (2010). *ANSYS FLUENT User's Guide*. Canonsburg.
- Ball, J. (2011, April 11). Wind Power Hits a Trough. *Wall Street Journal* .
- Basu, S., Vinuesa, J.-F., & Swift, A. (2008). Dynamic LES Modeling of a Diurnal Cycle. *Journal of Applied Meteorology and Climatology* , 47, 1156-1174.
- Bazilevs, Y., Hsu, M.-C., Akkerman, I., Wright, S., Takizawa, K., Henicke, B., et al. (2010). 3D Simulation of Wind Turbine Rotors at Full Scale. Part I: Geometry Modeling and Aerodynamics. *International Journal for Numerical Methods in Fluids* .
- Bazilevs, Y., Hsu, M.-C., Kiendl, J., Wüchner, R., & Bletzinger, K.-U. (2011). 3D Simulation of Wind Turbine Rotors at Full Scale. Part II: Fluid-Structure Interaction Modeling with Composite Blades. *International Journal for Numerical Methods in Fluids* , 65, 236-253.
- Blackadar, A. K. (1957). Boundary Layer Wind Maxima and their Significance for the Growth of Nocturnal Inversions. *Bulletin American Meteorological Society* , 38 (5), 283-290.
- Brown, R. E. (2000). Rotor Wake Modeling for Flight Dynamic Simulation of Helicopters. *AIAA Journal* , 38, 57-63.

- Brown, R. E., & Line, A. J. (2005). Efficient High-Resolution Wake Modeling Using the Vorticity Transport Equation. *AIAA Journal* , 43, 1434-1443.
- Calaf, M., Meneveau, C., & Meyers, J. (2010). Large Eddy Simulation Study of Fully Developed Wind-Turbine Array Boundary Layers. *Physics of Fluids* , 22.
- Christiansen, M. B., & Hasager, C. B. (2006). Using Airborne and Satellite SAR for Wake Mapping Offshore. *Wind Energy* , 9, 437-455.
- Clarke, R. H., Dyer, A. J., Brook, R. R., Reid, D. G., & Troup, A. J. (1971). The Wangara Experiment: Boundary Layer Data. *Division of Meteorological Physics Technical Paper* , 19, 316.
- Elliott, D. L., Holladay, C. G., Barchet, W. R., Foote, H. P., & Sandusky, W. F. (1986). *Wind Energy Resource Atlas of the United States*. United States Department of Energy. Richland: Pacific Northwest Laboratory.
- Emeis, S. (2010). Meteorological Explanation of Wake Clouds at Horns Rev Wind Farm. *Deutsches Windenergie Institut Magazin* , 37, 52-55.
- Fletcher, T. M., & Brown, R. E. (2010). Simulation of Wind Turbine Wake Interaction Using the Vorticity Transport Model. *Wind Energy* , 13, 587-602.
- Frandsen, S., Barthelmie, R., Pryor, S., Rathmann, O., Larsen, S., Højstrup, J., et al. (2006). Analytical Modelling of Wind Speed Deficit in Large Offshore Wind Farms. *Wind Energy* , 9 (1-2), 39-53.
- Glauert, H. (1935). Airplane propellers. In W. F. Durand (Ed.), *Aerodynamic Theory* (Vol. 4, pp. 169-360). Berlin: Julius Springer.

- Gottschall, J., & Peinke, J. (2007). Stochastic Modelling of a Wind Turbine's Power Output with Special Respect to Turbulent Dynamics. *Journal of Physics: Conference Series* , 75.
- Griffin, D. A. (2002). *Blade System Design Studies Volume I: Composite Technologies for Large Wind Turbine Blades*. Global Energy Concepts, LLC, Krikland.
- Hahm, T., & Wußow, S. (2006). Turbulent Wakes in Wind Farm Configuration. *EWEC Proceedings*.
- Hansen, M. O. (2008). *Aerodynamics of Wind Turbines* (2nd Edition ed.). London: Earthscan.
- Heyliger, P., Venayagamoorthy, S. K., Wilson, J., & Davis, C. (2011). *Coupled Structural Dynamic-Aerodynamic Behavior of Multiple Turbines: Influences Within Large Wind Farms*. Colorado State University. Unpublished.
- James, I. N. (1994). *Introduction to Circulating Atmospheres*. New York: Cambridge University Press.
- Jones, W. P., & Launder, B. E. (1972). The Prediction of Laminarization with a Two-Equation Model of Turbulence. *International Journal of Heat and Mass Transfer* , 15 (2), 301-314.
- Jonkman, J. M., & Buhl Jr., M. L. (2005). *FAST User's Guide*. National Renewable Energy Laborator.
- Jonkman, J., Butterfield, S., Musial, W., & Scott, G. (2009). *Definition of a 5-MW Reference Wind Turbine for Offshore Development*. National Renewable Energy Laboratory.

- Joshi, J. B., Nere, N. K., Rane, C. V., Murthy, B. N., Mathpati, C. S., Patwardhan, S. W., et al. (2011). CFD Simulation of Stirred Tanks: Comparison of Turbulence Models. Part I: Radial Flow Impellers. *The Canadian Journal of Chemical Engineering* , 89, 23-82.
- Leishman, J. G. (2006). *Principles of Helicopter Aerodynamics*. New York: Cambridge University Press.
- Lettau, H. (1969). Note on Aerodynamic Roughness-Parameter Estimation on the Basis of Roughness-Element Description. *Journal of Applied Meteorology* , 8, 828-832.
- Madsen, H. A., Mikkelsen, R., Øye, S., Bak, C., & Johansen, J. (2007). A Detailed Investigation of the Blade Element Momentum (BEM) Model Based on Analytical and Numerical Results and Proposal for Modifications of the BEM Model. *Journal of Physics: Conference Series*, 75.
- McGowan, J. G. (2000). Windpower: A Turn of the Century Review. *Annual Review of Energy and the Environment* , 25, 147-197.
- Menter, F. R. (2009). Review of the Shear-Stress Transport Turbulence Model Experience from an Industrial Perspective. *International Journal of Computational Fluid Dynamics* , 23 (4), 305-316.
- Menter, F. R. (1994). Two-Equation Eddy-Viscosity Turbulence Models for Engineering Applications. *AIAA Journal* , 32 (8), 1598-1605.
- Meyers, J., & Meneveau, C. (2011). Optimal Turbine Spacing in Fully Developed Wind Farm Boundary Layers. *Wind Energy* .

- Montavon, C. (1998). Validation of a Non-Hydrostatic Numerical Model to Simulate Wind Fields Over Complex Topography. *Journal of Wind Engineering and Industrial Aerodynamics* , 74-76, 273-282.
- Moriarty, P. J., Holley, W. E., & Butterfield, S. (2002). Effects of Turbulence Variation on Extreme Loads Prediction for Wind Turbines. *ASME Journal of Solar Energy Engineering* , 124, 387-395.
- Orszag, S. A., Staroselsky, I., Flannery, W. S., & Zhang, Y. (1996). Introduction to Renormalization Group Modeling of Turbulence. In T. B. Gatski, M. Y. Hussaini, & J. L. Lumley (Eds.), *Simulation and Modeling of Turbulent Flows* (pp. 155-184). New York: Oxford University Press, Inc.
- O'Sullivan, J. P., Archer, R. A., & Flay, R. G. (2011). Consistent Boundary Conditions for Flows Within the Atmospheric Boundary Layer. *Journal of Wind Engineering and Industrial Aerodynamics* , 99, 65-77.
- Pope, S. B. (2010). *Turbulent Flows*. New York: Cambridge University Press.
- Porté-Agel, F., Wu, Y.-T., Lu, H., & Conzemius, R. J. (2011). Large-eddy Simulation of Atmospheric Boundary Layer Flow Through Wind Turbines and Wind Farms. *Journal of Wind Engineering and Industrial Aerodynamics* , 99, 154-168.
- Saiki, E. M., Moeng, C.-H., & Sullivan, P. P. (2000). Large-Eddy Simulation of the Stable Stratified Planetary Boundary Layer. *Boundary-Layer Meteorology* , 95, 1-30.
- Shih, T.-H., Liou, W. W., Shabbir, A., Yang, Z., & Zhu, J. (1995). A New k- ϵ Eddy viscosity Model for High Reynolds Number Turbulent Flows. *Computers Fluids* , 24 (3), 227-238.

- Sullivan, P. P., & Patton, E. G. (2011, October). The Effect of Mesh Resolution on Convective Boundary Layer Statistics and Structures Generated by Large-Eddy Simulation. *Journal of the Atmospheric Sciences* , 2395-2415.
- Tachos, N. S., Filios, A. E., & Margaritis, D. P. (2010). A Comparative Numerical Study of Four Turbulence Models for the Prediction of Horizontal Axis Wind Turbine Flow. *Journal of Mechanical Engineering Science* , 224, 1973-1979.
- TPI Composites, Inc. (2004). *Innovative Design Approches for Large Wind Turbine Blades*. Warren: WindPACT Blade System Design Studies.
- USDOE. (2008). *20% Wind Energy By 2030*. United States Department of Energy.
- Wilcox, D. C. (1988). Multiscale Model for Turbulent Flows. *AIAA Journal* , 26 (11), 1311-1320.